

Nonlinear modelling and bifurcation analysis of the coupled dynamics of the offshore wind turbine with the tension leg floating platform

Soheil Ghabraei, * Hamed Moradi

Department of Mechanical Engineering, Sharif University of Technology, PO Box 11155-9567

Tehran, Iran, Tel: (+98) 21-66165545, Fax: (+98) 21-66000021

hamedmoradi@sharif.edu

Abstract

The present article investigates the coupled nonlinear dynamics of the offshore wind turbine with the floating tension leg platform through numerical methods. The NREL 5MW wind turbine installed on MIT/NREL Tension Leg Platform (TLP) is chosen as the floating offshore wind turbine. The offshore wind turbine equation of motion is derived using Hamilton's Principle, considering the floating platform surge, heave, and wind turbine's tower transverse motions. The wind turbine tower is modeled using the Euler-Bernoulli beam theory, and the effects of the platform surge and heave motions have been considered. Then, the Galerkin method is applied to the derived partial differential equations of motion of the tower to reduce them to a set of nonlinear ordinary differential equations. Afterward, by utilizing direct time integration, the effects of the frequency and amplitude of wave forcing and the length of the mooring lines on the floating wind turbine's global dynamics are studied. Finally, results are depicted as the frequency response curves and the Poincare maps' bifurcation diagrams. The phase-plane portraits, Poincare maps, and Fast Fourier Transforms (FFTs) highlight points of interest in the parameter space.

Keywords: Floating offshore wind turbine; Wave loading; Nonlinear vibrations; Frequency response; Bifurcation; Poincare' map section.

1. Introduction

Wind electricity generation will flourish to fulfill the global demand for clean, carbon-free electrical energy generation. In the offshore areas, the wind blows steadier more vigorously than in the lands. Inevitably, a large portion of generating clean, renewable, carbon-free wind energy will be harvested from the offshore areas. In the near future, the offshore wind farm will deliver electricity to the power grid and produce hydrogen from the seawater. The produced hydrogen will be burned in power plants to provide the peak grid demand. Unfortunately, most offshore wind energy is in areas with more than 50m water depths, which makes the traditional bottom fixed platforms, such as the jacket and monopile, unfeasible solutions. Therefore, inspired by the technologies developed in the previous decades in the offshore oil and gas industries, spar-buoy, Tension Leg Platform (TLP), and barge floating platforms are devised to deploy wind turbines in offshore areas. However, offshore wind energy on a floating platform is a new technology with difficulties and complexity [1].

Installation of wind turbines in offshore areas has some benefits, such as eliminating the visual and sound pollution of the wind turbines from urban areas, reducing some logistical challenges such as the narrow roadways or tunnels, and feasibility of transport and installation of enormous multimegawatt wind turbines. However, implementing wind turbines in offshore areas on floating platforms presents many new challenges. Any changes in loads exerted by waves or in the length of the mooring lines change the dynamics of the offshore floating wind turbine. The exerted load on the offshore floating wind turbine changes according to the working condition; for example, in a hurricane, the amplitude of the exerted loads due to the wave or wind will significantly increase. The length of the mooring line may change to install the floating platform in the sea with different depths. These changes alter the dynamics of the offshore floating wind turbine. They may increase the probability of undesired vibrations and consequently lead to the structure collapse due to the structure instabilities or fracture due to the low and high cycle fatigue. Accordingly, studying the dynamics of offshore wind turbines is a significant challenging problem.

Three floating concepts are proposed for the offshore wind turbine: spar-buoy, TLP, and barge floating platforms. The spar-Bouy floating platform has a simple design and excellent stability, but it is suitable for deep waters. Barge floating platforms are easy to assemble. However, constructing a barge-type floating platform consumes large amounts of steel. The TLP floating platform merits low mass and material consumption and provides excellent stability and considerably lower fatigue loads than the other concepts. It is suitable for a wide range of water depths. This platform consists of a floating platform moored to the seafloor via the tensioned tendons. The TLP is considerably stiff in the vertical direction (Heave) due to the tensioned mooring lines. Because the buoyancy of the platform held the TLP's tendons tensioned. The TLP provides excellent stability and robustness at the expense of the high loads on the mooring and anchoring system. Therefore, there are always concerns about the lifetime of the tendons.

Developing mathematical models to study the TLP dynamics attracts many researchers. on this subject, studying the TLP stochastic response [2], modeling a damaged TLP and studying its response [3], floating wind turbines dynamic analysis considering the hull flexibility [4], MIT/NREL Wind Turbine numerical modeling with TLP[5], setting up a experimental scaled model and the numerical model for the GICON®-TLP platform [6] smoothed particle hydrodynamics method implementation to study a TLP wind turbine [7], evaluating the TLP dynamic response under second-order waves [8], analyzing stability of TLP under marine environmental loads according to the connection angle of tendons [9], prediction of tendon tension of TLP platform using quasi-dynamic method [10] and dynamic stability of TLP tethers in case of vortex induced oscillations [11] have been done.

As aforementioned, the main shortcoming of the TLP is the high fatigue in the taught tendons that provide the stability of the TLP. The pretension tendons of the TLP suppress the wind and wave-exerted loads to the installed structure (in this case, the wind turbine). Consequently, the tendons are expected to fatigue failures due to the unceasing oscillating load of the wave and wind. Significant efforts have been conducted to study the vulnerability of the

TLP to fatigue failure, TLP fatigue reliability investigation [12], experimental evaluation of support structures fatigue strength using large-scale test setups [13], Analysis of structural damage by high-order wave loads to TLP [14], studying structural responses and fatigue damages of a submerged TLP wind turbine in wind and waves [15] and accurately assessment of both the impact behaviour and residual ultimate strength of dented TLP structures [16] have been done.

The dynamics of the TLP platform, as well as the offshore wind turbine with the TLP platform, have been studied by researchers in recent years. Square and triangular TLP dynamic study [17], investigating the effect of the added mass fluctuation on vertical vibrations of the TLP [18], dynamic modeling and loads analysis of an offshore floating wind turbine [19], developing the mathematical model and investigation exerted loads on the offshore wind turbine on a TLP [20,21], have been performed. Moreover, investigation of the tendon dynamics effects on TLP response in random seas [22], using analytical methods to study the coupled response of TLP [23], derive a closed-form solution for motions TLP surge motions using the homotopy perturbation method [24,25], studying the effect of the added mass on the offshore floating wind turbine heave vibrations [26], studying the coupled response of a TLP [27], Response amplitude mitigation of the TLP [28] dynamic analysis of offshore structures under seismic excitation [29] analyzing and horseshoes chaos controlling on TLP system [30] have been done.

However, the interaction between the floating platform and the wind turbine complicates the floating wind turbine. Experimental tests on the wave-induced response of a TLP supporting a 5 MW Wind Turbine [31] have been done in this regard.

Many efforts have been devoted to reducing the fatigue loads on the offshore floating wind turbine and increasing the stability and reliability of the floating offshore wind turbine through devising methods to attenuate the wind and wave-induced vibrations. Accordingly, vibration suppression of spar-type floating wind turbine using passive vibration controller [32,33], design and utilizing an optimal bidirectional mass damper for the offshore wind

turbines [34], and designing an active controller for vibration elimination of floating wind turbine [35–37] have been performed. In addition, using the dynamics vibration absorber to attenuate the oscillations of the offshore wind turbine with TLP [38], studying the effect of the modified TLP in response in regular waves [39] and active vibration control for flexible towers using reduced-order controller [40] have been carried out.

Wind turbine installation on a floating platform, such as a TLP platform, considerably increases the complexity of the wind turbine in comparison with the fixed-bottom wind turbine. Multi-directional wave loadings, the dynamics of the floating platform, and the connection between the floating platform and the wind turbine complicate the offshore floating wind turbine dynamics. The amplitude and the frequency of the wave loadings are indeterminate and stochastic. The length of the TLP tendons may deviate from its nominal values according to the water depth, which changes the platform surge and heave stiffness. Therefore, studying the offshore floating wind turbine dynamics is crucial to avoid the structural failure due to high-cycle or low-cycle fatigue and structural instabilities. According to the above discussions, in this research, at first, floating offshore wind turbine equations of motion are derived considering the coupling between the surge and heave degrees of freedom. The MIT/NREL TLP is the floating platform for the NREL 5MW wind turbine [41,42]. The wind turbine tower is modelled using the Euler-Bernoulli beam theory considering the effect of the motions in surge and heave direction in the tower equation of motion. Numeric simulations are carried out to investigate the validity of the developed governing equations. Then, the time histories are compared with those obtained from the National Renewable Energy Laboratory (NREL) FAST code [43]. Afterward, the system's steady-state response is studied by plotting the amplitude-frequency response curves for the wave loadings in the surge and heave degrees of freedom (DOF). Then, the effect of the forcing amplitude and change in the mooring lines' length on the floating wind turbine's global dynamics is studied by constructing the bifurcation diagrams and the Poincare maps. Then, attention is focused on interesting points of the bifurcation diagrams by plotting the Fast Fourier Transform (FFT) plots, phase plane portraits, and time histories.

2. Coupled nonlinear dynamic model of the offshore wind turbine

Fig. 1 represents a schematic view of the NREL 5MW wind turbine installed on the MIT/NREL TLP. The weight of the offshore floating wind turbine is less than the exerted buoyancy force. For that reason, the anchored mooring lines are in tension. As a result, the TLP is stiff in the heave DOF. Conversely, in the surge degrees of freedom, the TLP is compliant. The heave oscillations are due to the exerted vertical forces and surge degree of freedom. The pre-tensioned mooring lines, prone to high cycle and low cycle fatigue, are the primary source of the stability of the TLP. Therefore, the coupling between the surge and the heave degrees of freedom should be considered in modeling the TLP to have a better insight into the dynamics of the offshore wind turbine. The model will be more accurate in predicting the dynamics of the floating offshore wind turbine if the wind turbine tower is modeled as a continuous beam using the Euler-Bernoulli beam. The motions of the platform in the surge and heave directions impose forces on the wind turbine. Therefore, to consider the interaction between the wind turbine and the floating platform, the effect of the platform motions should be considered. In this section, the nonlinear dynamics of the floating wind turbine with a TLP floating platform will be driven by considering the mentioned concerns.

2.1 Equations of motion

Floating wind turbine schematic view is depicted in Fig. 1. Surge and heave degrees of freedom are considered to derive the governing equations of motion of the floating offshore wind turbine. ΔZ Equals the motions of the TLP platform in the heave DOF, which is composed of the heave displacement itself plus the heave displacements due to the coupling between the surge and heave DOF.

The wind turbine tower is modelled as a uniform Euler-Bernoulli beam to derive the floating offshore wind turbine equation of motion. The mass of the blades and nacelle is considered as a rigid body with mass and rotational inertia at the tip of the tower. In the following

equations, L is the wind turbine tower length, EI is the equivalent constant flexural rigidity, and ρA is the average linear mass density of the wind turbine tower. F_{wind_s} is the equivalent wind exerted load to the top of the tower in surge (horizontal) direction, F_{wind_h} is the equivalent wind exerted load to the top of the tower in heave (vertical) direction, M_{wind} is the equivalent wind exerted moment to the top of the tower, F_{wave_s} is the equivalent wave exerted load to the floating platform in surge (horizontal) direction and F_{wave_h} is the equivalent wave exerted load to the floating platform heave (vertical) direction. $u = u(x, t)$, $s = s(t)$, $h = h(t)$ denotes the transverse deflection of the wind turbine tower, platform motion in the surge (transverse) degree of freedom, and motions in heave degree of freedom, respectively. The kinetic energy of the floating wind turbine could be stated as:

$$\begin{aligned}
T = & \frac{1}{2} \int_0^l \rho A \left[\left(\frac{\partial s}{\partial t} + \frac{\partial u}{\partial t} + \frac{\partial h}{\partial t} \frac{\partial u}{\partial z} \right)^2 \right] dx + \frac{1}{2} m_p \left(\frac{\partial s}{\partial t} \right)^2 \\
& + \frac{1}{2} m_n \left(\left(\frac{\partial u}{\partial t}(t, l) \right)^2 + \left(\frac{\partial s}{\partial t} \right)^2 \right) + m_n \frac{\partial s}{\partial t} \frac{\partial u}{\partial t}(t, l) \\
& + \frac{1}{2} I_n \left(\frac{\partial^2 u}{\partial t \partial z}(t, l) \right)^2 + \frac{1}{2} I_p \left(\frac{\partial^2 u}{\partial t \partial z}(t, 0) \right)^2 \\
& + \frac{1}{2} (m_p + m_n + m_{tower}) \left(\frac{\partial h}{\partial t} \right)^2
\end{aligned} \tag{1}$$

$$\Pi_I = \frac{EI}{2} \int_0^l \left[\left(\frac{\partial^2 u}{\partial z^2} \right)^2 \right] dz + \frac{1}{2} K_{surge} s^2 + \frac{1}{2} (K_{heave} + K_{sh}) h^2 - \frac{1}{2} F_{wind_z} \int_0^l \left(\frac{\partial u}{\partial z} \right)^2 dz \tag{2}$$

The variation of the work done by the exerted wind and wave forces could be written as:

$$\begin{aligned}
W_I = & \int_0^l F_{wind_s} \delta(z-L) u dz + F_{wind_s} s + F_{waves} s + (F_{wave_z} + F_{wind_z}) h \\
& + EI \int_0^l M_{wind} \frac{\partial u}{\partial z} \delta(z-L) dz
\end{aligned} \tag{3}$$

The Equation of motion could be obtained using Hamilton's Principle as below:

$$\delta \int_{t_1}^{t_2} (\Pi - T - W) dt \quad (4)$$

where t_1 and t_2 are any two instants in time, and δ is the variation operator. After substituting Eq. (2) and Eq. (3) in Eq. (4) and finding variation regarding the system variables, then conducting integration by parts and simple mathematical manipulations, yield the following partial differential equations:

$$\begin{aligned} EI \frac{\partial^4 u}{\partial z^4} + \rho A \frac{\partial^2 u}{\partial t^2} = & -\rho A \left(\frac{\partial^2 s}{\partial t^2} + \frac{\partial^2 h}{\partial t^2} \frac{\partial u}{\partial z} + \frac{\partial h}{\partial t} \frac{\partial^2 u}{\partial z \partial t} \right) - \rho A \frac{\partial h}{\partial t} \frac{\partial}{\partial z} \left(\frac{\partial s}{\partial t} + \frac{\partial u}{\partial t} + \frac{\partial h}{\partial t} \frac{\partial u}{\partial z} \right) \\ & + F_{wind_z} \frac{\partial^2 u}{\partial z^2} + F_{wind_s} \delta(z-l) + EIM_{wind} \frac{\partial u}{\partial z} \delta(z-l) - m_n \left(\frac{\partial^2 s}{\partial t^2} + \frac{\partial^2 u}{\partial t^2}(t,l) \right) \\ & - I_n \left(\frac{\partial^2 u}{\partial t \partial z}(t,l) \frac{\partial u}{\partial z}(t,l) \right) \end{aligned} \quad (5a)$$

$$\begin{aligned} m_p \frac{\partial^2 s}{\partial t^2} + m_n \left(\frac{\partial^2 s}{\partial t^2} + \frac{\partial^2 u}{\partial t^2}(t,l) \right) \\ + \int_0^l \rho A \left(\frac{\partial^2 s}{\partial t^2} + \frac{\partial^2 u}{\partial t^2} + \frac{\partial^2 h}{\partial t^2} \frac{\partial u}{\partial z} + \frac{\partial h}{\partial t} \frac{\partial^2 u}{\partial z \partial t} \right) dz + k_{surge} s = F_{wind_s} + F_{wave_s} \end{aligned} \quad (5b)$$

$$\begin{aligned} (m_p + m_n + m_{tower}) \frac{\partial^2 h}{\partial t^2} + \int_0^l \rho A \frac{\partial u}{\partial z} \left(\frac{\partial^2 s}{\partial t^2} + \frac{\partial^2 u}{\partial t^2} + \frac{\partial^2 h}{\partial t^2} \frac{\partial u}{\partial z} + \frac{\partial h}{\partial t} \frac{\partial^2 u}{\partial z \partial t} \right) dx \\ + k_{heave} h + k_{hs} s + kh = F_{wave_s} \end{aligned} \quad (5c)$$

Eq. (5) represents the dynamics of the wind turbine's tower as a partial differential equation. Galerkin's method is implemented to discretize the equation of motions of the wind turbine tower to study the offshore wind turbine dynamics. Therefore, the following expansion is used:

$$u = \sum_i U_i(x) \eta_i(t) \quad (6)$$

In Eq. (7), the $U(z)$ stands for the n -th eigenfunction for the transverse motions of the wind turbine tower, and $\eta(t)$ denotes the n -th generalized coordinate. The modal equation of the wind turbine tower transverse vibrations is obtained by multiplying Eq. (5a) by $U_i(x)$ and then integrated along the length of the blade; the reduced governing equations of the offshore wind turbine are achieved as follows [44]:

$$\begin{aligned}
\ddot{\eta}_i + \omega_i^2 \eta_i = & -\frac{d^2 s}{dt^2} \sum_{i=1}^m \left(\rho A \int_0^l U_i(z) dz \right) - \frac{d^2 h}{dt^2} \sum_{i=1}^m \left(\rho A \int_0^l U_i(z) \frac{dU_i(z)}{dz} dz \right) \\
& - \dot{\eta}_i \frac{dh}{dt} \sum_{i=1}^m \left(\rho A \int_0^l U_i(z) \frac{dU_i(z)}{dz} dz \right) \\
& - \frac{\partial h}{\partial t} \dot{\eta}_i \sum_{i=1}^m \left(\rho A \int_0^l U_i(z) \frac{dU_i(z)}{dz} dz \right) - \left(\frac{\partial h}{\partial t} \right)^2 \dot{\eta}_i \sum_{i=1}^m \left(\rho A \int_0^l U_i(z) \frac{d^2 U_i(z)}{dz^2} dz \right) \\
& - \frac{\partial h}{\partial t} \dot{\eta}_i \sum_{i=1}^m \left(\rho A \int_0^l U_i(z) \frac{dU_i(z)}{dz} dz \right) - \left(\frac{\partial h}{\partial t} \right)^2 \dot{\eta}_i \sum_{i=1}^m \left(\rho A \int_0^l U_i(z) \frac{d^2 U_i(z)}{dz^2} dz \right) \\
& - m_n \sum_{i=1}^m \left(\rho A \int_0^l U_i(z) \left(\frac{\partial^2 s}{\partial t^2} + \frac{d^2 U_i(z)}{dz^2} \delta(z-l) \right) dz \right) \\
& - I_n \dot{\eta}_i \sum_{i=1}^m \left(\rho A \int_0^l U_i(z) \left(\frac{dU_i(l)}{dz} (t, l) \right) dz \right) \\
& + EIM_{wind} \sum_{i=1}^m \left(\rho A \int_0^l U_i(z) \frac{dU_i(z)}{dz} \delta(z-l) dz \right)
\end{aligned} \tag{7a}$$

$$\begin{aligned}
& \left(m_p + m_n + \int_0^l \rho A dz + m_{padded_s} \right) \frac{\partial^2 s}{\partial t^2} + k_{surge} s \\
& + \left(m_n \sum_i U_i(l) + \int_0^l \rho A U_i(z) dz \right) \ddot{\eta}_i \\
& + \left(\sum_{i=1}^m \int_0^l \rho A \frac{dU_i(z)}{dz} dz \right) \frac{\partial^2 h}{\partial t^2} \eta_i \\
& + \left(\sum_{i=1}^m \int_0^l \rho A \frac{dU_i(z)}{dz} dz \right) \frac{\partial h}{\partial t} \dot{\eta}_i = 0
\end{aligned} \tag{7b}$$

$$\begin{aligned}
& (m_p + m_n + m_{tower}) \frac{\partial^2 h}{\partial t^2} + \left(\sum_{i=1}^m \int_0^l \rho A \frac{dU_i(z)}{dz} dz \right) \frac{\partial^2 s}{\partial t^2} \\
& + \left(\sum_{i=1}^m \int_0^l \rho A \frac{dU_i(z)}{dz} U_i(l) dz \right) \ddot{\eta}_i \\
& + \left(\sum_{i=1}^m \int_0^l \rho A \frac{dU_i(z)}{dz} \frac{dU_i(z)}{dz} dz \right) \frac{\partial^2 h}{\partial t^2} \eta_i \\
& + \left(\sum_{i=1}^m \int_0^l \rho A \frac{dU_i(z)}{dz} \frac{dU_i(z)}{dz} dz \right) \frac{\partial h}{\partial t} \dot{\eta}_i + k_{heave} h + k_{hs} s + kh = f_z
\end{aligned} \tag{7c}$$

In the above equation, m_{Padded_s} , m_{Padded_p} represents the hydrodynamic added mass.

2.2 Model verification

The floating offshore wind turbine is installed on a soft and compliant platform (in comparison with the bottom fixed wind turbine). Therefore, the contribution of the mode shapes with the high frequency in the dynamics of the wind turbine tower will not be significant [19]. Accordingly, for the sake of simplicity, only the first mode shape of the fore-and-aft vibrations of the wind turbine's tower is considered. Therefore, we have:

$$u(z, t) = \varphi_1(z) \eta(t) \tag{8}$$

where η is the generalized coordinates in the fore-and-aft direction, and $\varphi_i(z)$ is the mode shapes of a cantilever beam as [44]:

$$\varphi_i(z) = \frac{\cos\left(\beta_i \frac{z}{l}\right) - \cosh\left(\beta_i \frac{z}{l}\right) + \alpha_i \left(\sin\left(\beta_i \frac{z}{l}\right) - \sinh\left(\beta_i \frac{z}{l}\right) \right)}{\cos(\beta_i) - \cosh(\beta_i) + \alpha_i \left(\sin(\beta_i) - \sinh(\beta_i) \right)} \tag{9}$$

$$\alpha_i = -\frac{\cos(\beta_i) + \cosh(\beta_i)}{\sin(\beta_i) + \sinh(\beta_i)} \quad \beta_1 = 1.875104. \tag{10}$$

According to the reference [45], the equivalent stiffness matrix of the TLP platform could be written as:

$$\begin{bmatrix} K_{ss} & 0 \\ K_{hs} & K_{hh} \end{bmatrix} \tag{11}$$

where in the above equation:

$$K_{ss} = \frac{n(T_0 + \Delta T) \sin \theta}{s} \quad (12a)$$

$$K_{sh} = 0 \quad (12b)$$

$$K_{hh} = \frac{1}{4} \pi \rho D_c^2 + \frac{4AE}{L} \quad (12c)$$

$$K_{hs} = n(\Delta T \cos \theta - (1 - \cos \theta) T_0) \quad (12d)$$

where ΔT is the alteration in the tension of the TLP tendons, L is the length of the tendons,

$\theta = \frac{s}{L}$ equals the tilting angle tendons due to the surge motions, A is the cross-sectional area

of the tendons, $\frac{AE}{L}$ equals the extensional stiffness of the tendons, ρ stands for the water

density, D_c represents the column of TLP. ΔT could be expressed as:

$$\Delta T = \left(\sqrt{u_l^2 + L^2} - L \right) K_0 = \left(\sqrt{\left(\frac{u_l}{L} \right)^2 + 1} - 1 \right) LK_0 \quad (13)$$

Using Tylor expansion, we know:

$$\left(\frac{1}{2} \left(\frac{s}{L} \right)^2 + 1 - 1 \right) LK_0 = \frac{1}{2} \left(\frac{s}{L} \right)^2 LK_0 \quad (14)$$

.Using the Taylor series for expansion about $\theta = \frac{s}{L} \approx 0$ triangular terms in Eq. (12) could be

approximated as:

$$\sin \theta \approx \frac{s}{L} \quad (15a)$$

$$\cos \theta = \frac{L}{\sqrt{s^2 + L^2}} \approx 1 - \frac{1}{2} \left(\frac{s}{L} \right)^2 \quad (15b)$$

By substituting Eq. (14) and Eq. (15) in Eq. (12), and by simple mathematical manipulations one has:

$$K_{ss} = 4 \left(\frac{T_0}{L} + \frac{AE}{2L^3} x^2 \right) \quad (16a)$$

$$K_{hh} = \frac{1}{4} \pi \rho D_c^2 + \frac{4AE}{L} \quad (16b)$$

$$K_{hs} = \frac{4(A_t E - T_0)}{2L} \left(\frac{s}{L} \right) - \frac{4A_t E}{4L} \left(\frac{s}{L} \right)^3 \quad (16c)$$

Even though the derived governing equations of motion of the offshore wind turbine are developed based on validated approaches, the derived governing equations should be validated to ensure the following steps' validity. National Renewable Energy Laboratory (NREL) FAST code, validated by many experimental examinations [46,47], is an efficient tool to solve the floating wind turbine dynamics. FAST code utilizes Aerodyn, Hydrodyne, and MoorDyn to calculate the exerted forces from the wind, wave, and mooring lines, respectively. The Aerodyn code utilize the Element Momentum theory to estimate the wind-exerted forces [48]. Wave-induced forces calculated by potential flow theory and Morison's Equation in Hydrodyne code [49]. The overall external exerted force on the floating platform could be expressed as [49]:

$$\mathbf{F}_{exerted} = -\mathbf{M}_{added} \mathbf{q} + \mathbf{F}_{wave} + \mathbf{F}_{mooring} \quad (17)$$

where the $\mathbf{F}_{exerted}$ is a vector of the exerted forces to the platform, \mathbf{M}_{added} is a matrix whose components represent the hydrodynamic added mass of the system, \mathbf{F}_{wave} is the vector representing the exerted wave forces excluding the added mass forces, and $\mathbf{F}_{mooring}$ is the vector of applied force by the mooring lines. The forces exerted on the floating platform are calculated using FAST code, as depicted in Fig. 2. In Fig. 2, the time history of the exerted loads in the heave and surge directions to the top of the tower and its spectral decomposition have been shown. The spectral decomposition is obtained via the FFT by applying the Hanning window and subtracting the mean value. Similarly, the time histories of exerted loads to the platform in the heave and surge directions are depicted in Fig. 3. The mean values of the

signals are subtracted to calculate the spectra. The exerted force's mean value in the surge direction results in the platform's static displacement. In the heave direction, the mean value of the exerted force equals the tower weight and is approximately equal to the buoyancy force.

According to Table.1, in which the main parameters of the MIT/NREL offshore floating wind turbine are presented, the stiffness matrix of the platform is calculated. According to Table.2, the averaged value of the EI flexural rigidity is calculated by equivalenting the wind turbine tower with a cantilever beam with a constant cross-section using the equation:

$$EI_{eq} = \frac{L}{3 \times \int_0^L \int_0^L \int_0^L \frac{I \times dx}{EI(x)} dx dx dx} = 464.53 \times 10^9 \text{ N.m}^2 \quad (18)$$

In the above equation, EI_{eq} is the flexural rigidity of the equivalent beam with a constant cross-section. Mass density is calculated via the:

$$\rho A = \frac{M_{Tower}}{L} \quad (19)$$

According to the calculated parameters, the developed governing equations of the motion should be verified. Therefore, the time histories obtained through the numerical simulation of Eq. (7) are compared with the results obtained from the FAST V8.0 code simulations. The JONSWAP spectrum with a significant wave height of 6m and a peak spectral wave period of 10 s is utilized to generate an irregular wave profile. The offshore floating wind turbine is considered exposed to the wind with a uniform wind profile with a speed of 15 m/s at 90m. In this regard, according to the Table 1, 2, and 3, the parameters of Eq. (7) are assigned as

$$M_{tower} = 347460 \text{ kg}, \quad M_{platform} = 8600000 \text{ kg}, \quad K_{hh} = 8.2 \times \frac{10^7 \text{ N}}{m}, \quad K_{ss} = 6.147 \times 10^8 \text{ N/m}.$$

The comparison of the obtained time histories for the developed model in Eq. (7) with the time histories calculated via the FAST code is depicted in Fig. 4 . Accordingly, the developed model has an acceptable accuracy in representing the dynamic of the floating offshore wind turbine. According to Fig. 4, the suggested model demonstrates acceptable accuracy when predicting

the vertical oscillations of the floating offshore wind turbine. According to the calculated stiffness, the natural frequency of the floating offshore wind turbine can be calculated through the following equations:

$$\omega_{surge} = \sqrt{\frac{K_s}{m_P + m_{P_{added_s}} + m_{WT}}} \quad (20)$$

$$\omega_{heave} = \sqrt{\frac{K_h}{m_P + m_{P_{added_h}}(\infty) + m_{WT}}}$$

In the above equation, $m_{P_{added_s}}$ and $m_{P_{added_h}}$ represent the added mass in the surge and the heave DOF. Corresponding values equal to its value at a frequency equal to ∞ , are assigned according to Fig. 5. Using Eq. (20), the natural period of the floating offshore wind turbine is calculated as $2.6s$ and $60s$ in the heave and surge degrees of freedom.

3 Amplitude-frequency responses for sinusoidal sweep

In this section, to investigate the offshore wind turbine's dynamic, the impact of the variations of the primary parameters, including the magnitude of the exerted wave force in the surge DOF, the impact of the coupling stiffness, K_{hs} , and the impact of the damping in the surge DOF on the frequency response of the offshore wind turbine is studied. According to Eq. (17), the value of the coupling stiffness depends on the length of the tendon L , which may change to comply with the sea depth. The K_{ss} and the K_{hs} have nonlinear terms. Therefore, the effect of the wave forcing amplitude in the surge direction, the consequence of the variation in the coupling stiffness, K_{hs} , and the platform damping in the surge DOF have interesting phenomena. In this regard, the frequency response curve is calculated by plotting the system amplitude versus the frequency of the excitation force [51–53]. The frequency increment is set to $\Delta\omega = 0.0001$ during the calculation of the frequency response curve. The frequency response curve for the surge, heave, and deflection of the wind turbine's tower is depicted in Fig. 6 for the wave forcing in the surge direction while the other excitations are set to zero. Accordingly,

it can be deduced that as the magnitude of the wave force is raised, the amplitude of the motions increases.

Moreover, the dynamics of the system exhibit more complexity. As shown in Fig. 6, more jump phenomena were seen in the frequency response as the forcing amplitude increased. Black arrows indicate the jump phenomenon and its direction. For the forcing amplitude $20F_{wave}$, two jump phenomena are observed for $\omega = 0.0558 \text{ Hz}$ and $\omega = 0.2203 \text{ Hz}$; however, for the forcing amplitude F_{wave} , the jump phenomenon occurs only for $\omega = 0.1157 \text{ Hz}$. Another interesting observed phenomenon is the frequency shift at which the jump phenomena occur as the forcing amplitude shifts. For the forcing value F_{wave} , the jump phenomenon occurs at $\omega = 0.117$, but as the forcing amplitude increases to, the frequency of the jump $20F_{wave}$ phenomenon shifts to 0.2202 Hz .

The damping effect on the surge motions' frequency response of the offshore wind turbine is shown in Fig. 7. As expected, the magnitude of the vibrations decreases as the damping increases.

The effect of increasing the coupling stiffness between the surge and heave motion on the dynamics of the offshore wind turbine is studied in Fig. 8. The increase of the K_{hs} occurs if the length of the mooring line decreases from its nominal values. As it is observed, the effect of the coupling stiffness on the surge motion is not significant. However, as the coupling stiffness increases, the heave motions' amplitude increases considerably. The dynamics of the tower deflection is also affected by the increase in coupling stiffness. However, it is not significant.

4 Bifurcation Diagrams & Analysis

This section is devoted to studying the effect of the variation in the main offshore wind turbine's parameters on its dynamics by plotting the bifurcation diagrams and the Poincare maps. A sudden change in the system response to a change in a parameter is called the bifurcation phenomenon. In order to plot the bifurcation diagram, a certain measure of the system's generalized coordinate is plotted against the variation of one of the system's parameters, called the bifurcation parameter. Throughout this section, $f_s = \frac{F_{wave_s}}{2.5 \times 10^5}$, 2.5×10^5 is the maximum amplitude observed in the spectrum of the exerted wave loading to the floating platform in the surge direction, according to Fig. 3. Similarly, the $f_h = \frac{F_{wave_h}}{1.5 \times 10^5}$, 1.5×10^5 is the maximum amplitude observed in the spectrum of the exerted wave loading to the floating platform in the heave direction, according to Fig. 3.

The effect of the wave force amplitude in the surge DOF on the dynamics of the offshore wind turbines is studied by plotting the bifurcation of the Poincare section in Fig. 9 and setting other excitation forces to zero. As is seen in Fig. 9, a sudden increase in the amplitude occurs in 1.974. Similarly, at the $f_s = 51.08$, a jump in the amplitude of the vibration occurs. Only periodic attractors are observed in the range of $f_s = [0.00171.64]$. However, for $f_s > 71.64$, chaotic motion is observed. Typical chaotic characteristics of the motion is depicted in Fig. 10 for $f_s = 83$.

The effect of the wave forcing amplitude in the heave direction on the dynamics of the offshore wind turbines is depicted in Fig. 11. There is only one attractor until, $f_h = 9.056$ where the motion exhibits chaotic characteristics. Afterward, until the $f_h = 22.33$ the system's dynamics exhibits the periodic motion with multiple periodic attractors, the number of which changes as the forcing amplitude changes. The system exhibits chaotic motion in the interval $f_h = [22.33 26.09]$. However, there are some narrow intervals with periodic motions with

multiple attractors. In the interval $f_h = [26.09\ 39.28]$, system characteristics changes from the chaotic motion to the periodic motions with multiple attractors, the number of which changes as the forcing amplitude changes. In the interval $f_h = [39.28\ 40]$, the system again exhibits chaotic motions with narrow intervals of periodic motions. The characteristics of typical chaotic motion is depicted in Fig. 12 for $f_h = 9.375$.

The equivalent stiffness of the floating platform would reduce from its designed nominal values if the length of the mooring line increased. In Fig. 13, the impact of the 30% length increase of the TLP mooring lines on the dynamics of the offshore wind turbine is studied. As shown in Fig. 13, only one periodic attractor exists for the interval $f_s = [0\ 74.26]$. However, some jumps in the amplitude of the vibration exist. The system exhibits quasi-periodic dynamics for the interval $f_s = [74.26\ 91.65]$. Compared with Fig. 9, which is the original system, the chaotic motion is postponed with the reduction in the stiffness of the mooring lines. Typical quasi-periodic characteristics of the motion is demonstrated in Fig. 14 for $f_s = 85$

In Fig. 15, the effect of 30% length increase of the TLP mooring lines on the system dynamics in the case of wave loadings in the heave (vertical) direction is investigated. Compared with Fig. 11, the system's dynamics change with this increase in the length of the mooring lines. The most important changes in the dynamics of the offshore wind turbine are the occurrence of the chaos [54] for the interval and the chaotic motion $f_s = [16.8\ 18.24]$ elimination for $f_h = 9.375$. The characteristics of typical chaotic motion is demonstrated in Fig. 16 for $f_s = 17.3$.

It is interesting how the offshore wind turbine dynamics are affected if the length of the mooring line is reduced. According to Eq. (12), as the tendons length is reduced, the equivalent stiffness of the TLP will increase. The dynamics of the offshore wind turbine are investigated

in the case where the length of the mooring lines is decreased by 50% from its nominal values through the plotting Poincare points bifurcation diagrams, which are depicted in Fig. 17. Accordingly, in comparison with Fig. 9, the chaotic motions occur in considerably lower f_s values. The chaotic motion is observed for the interval $f_s = [17.235.4]$. However, there are narrow intervals with periodic motions with multiple attractors. In the interval $f_s = [35.443.3]$, the periodic motion with three attractors is seen, but there are more significant number of periodic attractors for narrow intervals. For the interval $F_s = [44.464]$, the regions with chaotic and periodic motion with multiple attractors are again seen.

Interestingly, for the values $f_s > 79.7$, system has only one periodic attractor. Accordingly, the system's dynamics significantly change with the increase in stiffness, and the chance of chaotic motions is increased for smaller f_s . A typical period-3 oscillation for $f_s = 39.84$ characteristics is shown in Fig. 18.

Fig. 19 depicts the mooring lines' length reduction effect on the Poincare point's bifurcation. Compared with Fig. 11, the stiffer mooring lines considerably affect the system's dynamics. For example, there is a chaotic region for $f_h = [16.2717.93]$, where, according to Fig. 11, for nominal TLP there are periodic attractors. The characteristics of typical chaotic motion is demonstrated in Fig. 20 for $f_h = 16.2$.

Finally it should be mentioned that in this section, and through the analysis of parameters' influence, to demonstrate and study the nonlinear phenomena (such as quasi-periodic oscillations, chaotic oscillations and etc.), large values for parameters are also used (for only analytical purposes, similar to several investigations in this area, like those in [54]). However, large theoretical values of some parameters may not occur in reality or in the case of the consequence of large vibration amplitudes, the structure of the offshore wind turbine may

collapse under such condition. Therefore, the results of this investigation can be also used as some preliminary remarks before the implementation of the design in practice.

Conclusions

This paper studies the nonlinear dynamics of the floating offshore wind turbine. In the first step, the floating offshore wind turbine governing equation is derived considering the coupling between the surge and heave degrees of freedom. The MIT/NREL TLP is the floating platform for The NREL 5MW wind turbine. The wind turbine's tower is modelled using the Euler-Bernoulli beam theory, which considers the effects of the floating platform movements in the heave and surge directions. Then, the derived model is verified via FAST code. Afterward, the floating offshore wind turbine dynamics are studied by plotting the amplitude-frequency response curves:

- The dynamics of the offshore floating wind turbine are considerably affected by the amplitude of the wave forcing in the surge direction.
- Adding damping reduces the amplitude of the wave-induced motion considerably.
- The coupling stiffness between the surge and heave directions, K_{hs} , affects the motion dynamics in the surge directions. By increasing the stiffness value of K_{hs} to 4 times, the range of motion in heave direction can be increased by about 5 times. The value of K_{hs} will increase by reducing the length of the mooring lines of the TLP floating platform. Therefore, the change in the length of the mooring lines will require a more detailed investigation.

Afterward, the forcing amplitude effect and the mooring lines length change on the floating wind turbine's global dynamics are studied by constructing the bifurcation diagrams and Poincare maps and plotting the FFT plots, phase plane portraits, and time histories in the interesting points. According to the carried out numerical results, the subsequent remarks are concluded:

- As the wave forcing amplitude in the surge and heave directions is increased, the chance of the quasi-periodic and chaotic oscillations is increased.
- The quasi-periodic and chaotic oscillations occur in the lower amplitude of the wave forcing in the heave direction compared with the wave forcing in the surge direction.
- The chance of the quasi-periodic and chaotic oscillations is increased as the TLP mooring line length is reduced.

Therefore, it is strongly advised to investigate the floating offshore wind turbine dynamics according to the environmental conditions, such as the wave height and the length of the tendons (mooring lines), to avoid devastating quasi-periodic and chaotic oscillations. This investigation suggests that other concepts of floating offshore wind turbines could also be analyzed similarly

Acknowledgment

The authors acknowledge the “Research Office of Sharif University of Technology, Tehran, Iran” for supporting this research through the grant program # QA010910.

Conflict of Interest

None declared.

References

1. Collu, M. and Borg, M., “11 - Design of floating offshore wind turbines”, In *Offshore Wind Farms*, C. Ng and L. Ran, Eds., Woodhead Publishing, pp. 359–385 (January 1, 2016).
2. Ahmad, S., “Stochastic TLP response under long crested random sea”, *Computers & Structures*, **61**(6), pp. 975–993 (1996). DOI: 10.1016/0045-7949(96)00188-5
3. Tabeshpour, M. R., Ahmadi, A., and Malayjerdi, E., “Investigation of TLP behavior under tendon damage”, *Ocean Engineering*, **156**, pp. 580–595 (2018). DOI:10.1016/j.oceaneng.2018.03.019.

4. Silva de Souza, C. E. and Bachynski, E. E., “Effects of hull flexibility on the structural dynamics of a tension leg platform floating wind turbine”, *Journal of Offshore Mechanics and Arctic Engineering*, **142**(011903) (2019). DOI: 10.1115/1.4044725.
5. Vardaroglu, M., Gao, Z., Avossa, A. M., et al., “Numerical modelling of the MIT/NREL TLP wind turbine and comparison with the experimental results”, *Journal of Physics: Conference Series*, **1669**(1), p. 012015 (2020). DOI:10.1088/1742-6596/1669/1/012015.
6. Walia, D., Schünemann, P., Hartmann, H., et al., “Numerical and physical modeling of a tension-leg platform for offshore wind turbines”, *Energies*, **14**(12) (2021). DOI:10.3390/en14123554.
7. Tagliafierro, B., Karimirad, M., Martínez-Estévez, I., et al., “Numerical assessment of a tension-leg platform wind turbine in intermediate water using the smoothed particle hydrodynamics method”, *Energies*, **15**(11) (2022). DOI: 10.3390/en15113993.
8. Wang, J., Luo, Y., Wang, Y., et al., “Dynamic response of tension leg platform with hydro-pneumatic tensioner under second-order waves and freak waves”, *Ocean Engineering*, **252**, p. 111261 (2022). DOI:10.1016/j.oceaneng.2022.111261.
9. Xu, X., Wei, N., and Yao, W., “The stability analysis of tension-leg platforms under marine environmental loads via altering the connection angle of tension legs”, *Water*, **14**(3) (2022). DOI:10.3390/w14030283.
10. Huang, W., Li, B., and Chen, X., “A new quasi-dynamic method for the prediction of tendon tension of TLP platform”, *Ocean Engineering*, **270**, p. 113590 (2023). DOI:10.1016/j.oceaneng.2022.113590.
11. Mitra, R. K., Mondal, S. S., and Banik, A. K., “Dynamic stability and control of vortex induced oscillations of tension leg platform tethers”, *Journal of Sound and Vibration*, **585**, p. 118442 (2024). DOI:10.1016/j.jsv.2024.118442.
12. Siddiqui, N. A. and Ahmad, S., “Fatigue and fracture reliability of TLP tethers under random loading”, *Marine Structures*, **14**(3), pp. 331–352 (2001). DOI:10.1016/S0951-8339(01)00005-3.
13. Schaumann, P., Böhm, M., and Schürmann, K., “Improvements in the fatigue design of support structures for offshore wind turbines”, *Steel Construction*, **14**(2), pp. 74–82 (2021). DOI:10.1002/stco.202000060.
14. Liu, J.-R., Zhao, Y.-S., He, Y.-P., et al., “Effects of second-order wave force on fatigue damage assessment of a TLP-type floating wind turbine”, p. ISOPE-I-20-1185 (2020).
15. Han, Y., Le, C., Zhang, P., Dang, L., et al., “Stochastic analysis of short-term structural responses and fatigue damages of a submerged tension leg platform wind turbine in wind and waves”, *China Ocean Engineering*, **35**(4), pp. 566–577 (2021). DOI:10.1007/s13344-021-0051-y.
16. Do, Q. T., Ghanbari-Ghazijahani, T., and Prabowo, A. R., “Developing empirical formulations to predict residual strength and damages in tension-leg platform hulls after a collision”, *Ocean Engineering*, **286**, p. 115668 (2023). DOI:10.1016/j.oceaneng.2023.115668.
17. Chandrasekaran, S. and Jain, A. K., “Dynamic behaviour of square and triangular offshore tension leg platforms under regular wave loads”, *Ocean Engineering*, **29**(3), pp. 279–313 (2002). DOI:10.1016/S0029-8018(00)00076-7.
18. Tabeshpour, M. R., Golafshani, A. A., and Seif, M. S., “Second-order perturbation added mass fluctuation on vertical vibration of tension leg platforms”, *Marine Structures*, **19**(4), pp. 271–283 (2006). DOI:10.1016/j.marstruc.2007.02.001.
19. Jonkman, J. M., *Dynamics modeling and loads analysis of an offshore floating wind turbine*, University of Colorado at Boulder (2007).
20. Matha, D., *Model development and loads analysis of an offshore wind turbine on a tension leg platform with a comparison to other floating turbine concepts: April 2009*, National Renewable Energy Lab.(NREL), Golden, CO (United States) (2010).
21. Robertson, A. N. and Jonkman, J. M., “Loads analysis of several offshore floating wind turbine concepts”, p. ISOPE-I-11-204 (2011).

22. Oyejobi, D. O., Jameel, M., Sulong, N. H. R., et al., “Investigation of tendon dynamics effects on tension leg platform response in random seas”, *Proceedings of the Institution of Mechanical Engineers, Part M: Journal of Engineering for the Maritime Environment*, **233**(4), pp. 1082–1102 (2019). DOI:10.1177/1475090218811718.
23. Tabeshpour, M. R. and Hedayatpour, R., “Analytical investigation of nonlinear heave-coupled response of tension leg platform”, *Proceedings of the Institution of Mechanical Engineers, Part M: Journal of Engineering for the Maritime Environment*, **233**(3), pp. 699–713 (2019). DOI:10.1177/1475090218776430.
24. Tabeshpour, M. R. and Shoghi, R., “Perturbation nonlinear response of tension leg platform under regular wave excitation”, *Journal of Marine Science and Technology*, **23**(1), pp. 132–140 (2018). DOI:10.1007/s00773-017-0461-y.
25. Shoghi, R. and Tabeshpour, M. R., “An approximate method for the surge response of the tension leg platform”, *Journal of Marine Science and Application*, **13**(1), pp. 99–104 (2014). DOI:10.1007/s11804-014-1223-4.
26. Ghabraei, S., Moradi, H., and Vossoughi, G., “Investigation of the effect of the added mass fluctuation and lateral vibration absorbers on the vertical nonlinear vibrations of the offshore wind turbine”, *Nonlinear Dynamics*, **103**(2), pp. 1499–1515 (2021). DOI:10.1007/s11071-020-06194-1.
27. Jin, R., Jiang, Y., Shen, W., et al., “Coupled dynamic response of a tension leg platform system under waves and flow at different heading angles: An experimental study”, *Applied Ocean Research*, **115**, p. 102848 (2021). DOI:10.1016/j.apor.2021.102848.
28. Tabeshpour, M. R. and Nikmehr, L., “Numerical and experimental study on dynamic response mitigation of tension leg platform using tuned mass damper”, *Journal of Ship Research*, **66**(04), pp. 265–276 (2022). DOI:10.5957/JOSR.06200039.
29. Yu, Y., Li, Z., Cheng, S., et al., “Dynamic response of deepwater tension leg platform under seismic ground motion and wave loading”, ISOPE, p. ISOPE-I (2021).
30. Ngounou, A., Feulefack, S. M., Tabejieu, L. A., et al., “Design, analysis and horseshoes chaos control on tension leg platform system with fractional nonlinear viscoelastic tendon force under regular sea wave excitation”, *Chaos, Solitons & Fractals*, **157**, p. 111952 (2022). DOI:10.1016/j.chaos.2022.111952.
31. Ren, Y., Shi, W., Venugopal, V., et al., “Experimental study of tendon failure analysis for a TLP floating offshore wind turbine”, *Applied Energy*, **358**, p. 122633 (2024). DOI:10.1016/j.apenergy.2024.122633.
32. Sarkar, S. and Fitzgerald, B., “Fluid inerter for optimal vibration control of floating offshore wind turbine towers”, *Engineering Structures*, **266**, p. 114558 (2022). DOI:10.1016/j.engstruct.2022.114558.
33. Lin, J., Wang, Y., Zhang, G., et al., “Novel tuned mass dampers installed inside tower of spar offshore floating wind turbines”, *Ocean Engineering*, **301**, p. 117412 (2024). DOI:10.1016/j.oceaneng.2024.117412.
34. Saghi, H., Ma, C., and Zi, G., “Bidirectional tuned liquid dampers for stabilizing floating offshore wind turbine substructures”, *Ocean Engineering*, **309**, p. 118553 (2024). DOI:10.1016/j.oceaneng.2024.118553.
35. Alkhoury, P., Ait-Ahmed, M., Soubra, A.-H., et al., “Vibration reduction of monopile-supported offshore wind turbines based on finite element structural analysis and active control”, *Ocean Engineering*, **263**, p. 112234 (2022). DOI:10.1016/j.oceaneng.2022.112234.
36. Jokar, H., Vatankhah, R., and Mahzoon, M., “Active vibration control of horizontal-axis wind turbine blades using disturbance observer-based boundary control approach”, *Engineering Structures*, **275**, p. 115323 (2023). DOI:10.1016/j.engstruct.2022.115323.
37. Yan, S., Wang, Y., Pang, F., et al., “Wind and wave-induced vibration reduction control for floating offshore wind turbine using delayed signals”, *Journal of Marine Science and Engineering*, **12**(7) (2024). DOI:10.3390/jmse12071113.

38. Z. Wu and Y. Li, “Platform stabilization and load reduction of floating offshore wind turbines using dynamic vibration absorbers”, *2018 Annual American Control Conference (ACC)*, pp. 1497–1502 (2018). DOI:10.23919/ACC.2018.8431066.
39. Song, J. and Lim, H.-C., “Study of floating wind turbine with modified tension leg platform placed in regular waves”, *Energies*, **12**(4) (2019). DOI:10.3390/en12040703.
40. Wen, X., Zhang, H., Chen, Z., et al., “Active vibration control for flexible towers based on displacement observation and reduced-order controller in modal space: Theory and experiment”, *Engineering Structures*, **311**, p. 118136 (2024). DOI:10.1016/j.engstruct.2024.118136.
41. Jonkman, J., “Definition of a 5-mw reference wind turbine for offshore system development” (2009).
42. Jonkman, J. M. and Matha, D., “Dynamics of offshore floating wind turbines—analysis of three concepts”, *Wind Energy*, **14**(4), pp. 557–569 (2011). DOI:10.1002/we.442.
43. Jonkman, J. M. and Buhl Jr, M. L., *FAST user’s guide—updated august 2005*, National Renewable Energy Lab.(NREL), Golden, CO (United States) (2005).
44. Rao, S. S., *Vibration of continuous systems*, John Wiley & Sons (2019).
45. Jain, A., “Nonlinear coupled response of offshore tension leg platforms to regular wave forces”, *Ocean Engineering*, **24**(7), pp. 577–592 (1997). DOI:10.1016/0029-8018(95)00059-3.
46. Guntur, S., Jonkman, J., Sievers, R., et al., “A validation and code-to-code verification of FAST for a megawatt-scale wind turbine with aeroelastically tailored blades”, *Wind Energy Science*, **2**(2), pp. 443–468 (2017). <https://doi.org/10.5194/wes-2-443-2017>
47. Popko, W., Huhn, M. L., Robertson, A., et al., “Verification of a numerical model of the offshore wind turbine from the alpha ventus wind farm within oc5 phase iii”, *OMAE2018*, Volume 10: Ocean Renewable Energy (2018). DOI:10.1115/OMAE2018-77589.
48. Jonkman, J. M., Hayman, G., Jonkman, B., et al., “AeroDyn v15 user’s guide and theory manual”, *NREL Draft Report*, **46** (2015).
49. Jonkman, J., Robertson, A., and Hayman, G., “HYDRODYN user’s guide and theory manual, nrel, 2014”, *Available online. Assessed on Dec* (2014).
50. Matha, D., “Modelling and loads & stability analysis of a floating offshore tension leg platform wind turbine”, *Master’s* (2009).
51. Khaniki, H. B., Ghayesh, M. H., Hussain, S., et al., “Effects of geometric nonlinearities on the coupled dynamics of CNT strengthened composite beams with porosity, mass and geometric imperfections”, *Engineering with Computers*, **38**(4), pp. 3463–3488 (2022). DOI:10.1007/s00366-021-01474-9.
52. Karimi, B. and Moradi, H., “Nonlinear kinematics analysis and internal resonance of wind turbine blade with coupled flapwise and edgewise vibration modes”, *Journal of Sound and Vibration*, **435**, pp. 390–408 (2018). DOI:10.1016/j.jsv.2018.08.017.
53. Belato, D., Weber, H. I., Balthazar, J. M., et al., “Chaotic vibrations of a nonideal electro-mechanical system”, *International Journal of Solids and Structures*, **38**(10), pp. 1699–1706 (2001). DOI:10.1016/S0020-7683(00)00130-X.
54. Nayfeh, A. H. and Balachandran, B., *Applied nonlinear dynamics: analytical, computational, and experimental methods*, John Wiley & Sons (2008).

Fig. 1. Floating wind turbine schematic view.....	7
Fig. 2. Time history and FFT of exerted force to the Top of the turbine (a) in surge direction (b) in heave direction	14
Fig. 3. Time history and FFT of exerted force to the platform (a) in surge direction (b)in heave direction	15
Fig. 4. Comparison of the time history of the motions of the FAST (blue solid line) and proposed model (red dashed line).	17
Fig. 5. Hydrodynamic added-mass coefficients of the TLP [50]	18
Fig. 6: Frequency response of the (a) surge motions of the offshore wind turbine (b) heave motion (c) deflection of the tower of the offshore wind turbine for increasing the wave forcing F_{wave_s}	21
Fig. 7: Frequency response of the (a) surge motions of the offshore wind turbine (b) heave motion (c) deflection of the tower of the offshore wind turbine for various damping in the surge direction.....	22
Fig. 8: Frequency response of the (a) surge motions of the offshore wind turbine (b) heave motion (c) deflection of the tower of the offshore wind turbine for increasing the coupling stiffness K_{hs}	23
Fig. 9: Bifurcation diagrams of Poincaré points for increasing the wave forcing amplitude in the surge direction for (a) surge motions of the offshore wind turbine (b) heave motion (c) deflection of the tower of the offshore wind turbine	26
Fig. 10: Chaotic oscillation for the floating offshore wind turbine at $f_s = 83$; (a) phase-plane diagram of the surge motions; (b) Poincaré section of the surge motions, (c) FFT of the surge motions and (d) time history of the surge motions.	27
Fig. 11: Bifurcation diagrams of Poincaré points for increasing the wave forcing amplitude in the heave direction for (a) surge motions of the offshore wind turbine (b) heave motion (c) deflection of the tower of the offshore wind turbine	28
Fig. 12: Chaotic oscillation for the floating offshore wind turbine at $f_h = 9.375$; (a) phase-plane diagram of the surge motion; (b) Poincaré section of the surge motion, (c) FFT of the surge motion and (d) time history of the surge motion.	29
Fig. 13: Bifurcation diagrams of Poincaré points for increasing the wave forcing amplitude in the surge direction with 30% increase in the length of the mooring lines for (a) surge motions of the offshore wind turbine (b) heave motion (c) deflection of the tower of the offshore wind turbine	31
Fig. 14: Quasi-periodic oscillation for the floating offshore wind turbine with 30% increase in the length of the mooring lines at $f_s = 85$; (a) phase-plane diagram of the surge motions; (b) Poincaré section of the surge motions, (c) FFT of the surge motions and (d) time history of the surge motions.....	32
Fig. 15: Bifurcation diagrams of Poincaré points for increasing the wave forcing amplitude in the heave direction with 30% increase in the length of the mooring lines for (a) surge motions of the offshore wind turbine (b) heave motion (c) deflection of the tower of the offshore wind turbine.....	33

Fig. 16: Chaotic oscillation for the floating offshore wind turbine with 30% increase in the length of the mooring lines at $f_h = 17.3$; (a) phase-plane diagram of the surge motion; (b) Poincaré section of the surge motion, (c) FFT of the surge motion and (d) time history of the surge motion..... 34

Fig. 17: Bifurcation diagrams of Poincaré points for increasing the wave forcing amplitude in the surge direction with 50% decrease in the length of the mooring lines for (a) surge motions of the offshore wind turbine (b) heave motion (c) deflection of the tower of the offshore wind turbine..... 36

Fig. 18: Periods-3 oscillation for the floating offshore wind turbine with 50% reduction in the length of the mooring lines at $f_s = 39.84$; (a) phase-plane diagram of the surge motions; (b) Poincaré section of the surge motions, (c) FFT of the surge motions and (d) time history of the surge motions..... 37

Fig. 19: Bifurcation diagrams of Poincaré points for increasing the wave forcing amplitude in the heave direction with 50% reduction in the length of the mooring lines for (a) surge motions of the offshore wind turbine (b) heave motion (c) deflection of the tower of the offshore wind turbine..... 39

Fig. 20: Chaotic oscillation for the floating offshore wind turbine with 50% reduction in the length of the mooring lines at $f_h = 16.2$; (a) phase-plane diagram of the surge motion; (b) Poincaré section of the surge motion, (c) FFT of the surge motion and (d) time history of the surge motion..... 40

Table. 1. Summary of the properties for the NREL 5 MW baseline wind turbine [41]..... 18

Table. 2. Distributed tower properties of the NREL 5 MW baseline wind turbine [41]..... 18

Table. 3. Summary of the properties for the MIT/NREL floating platforms [42]. 19

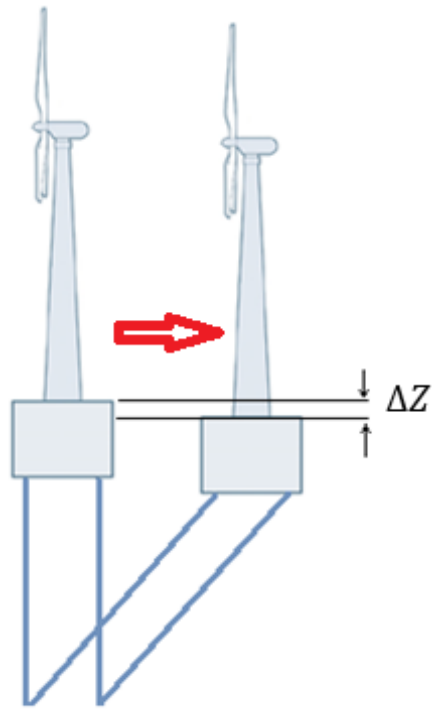


Fig. 1. Floating wind turbine schematic view

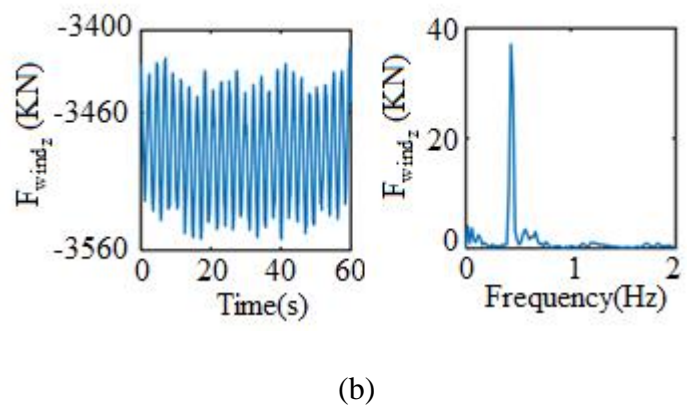
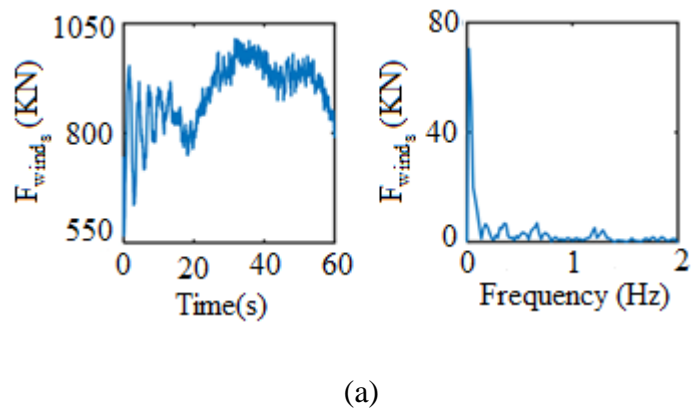


Fig. 2. Time history and FFT of exerted force to the Top of the turbine (a) in surge direction
(b) in heave direction

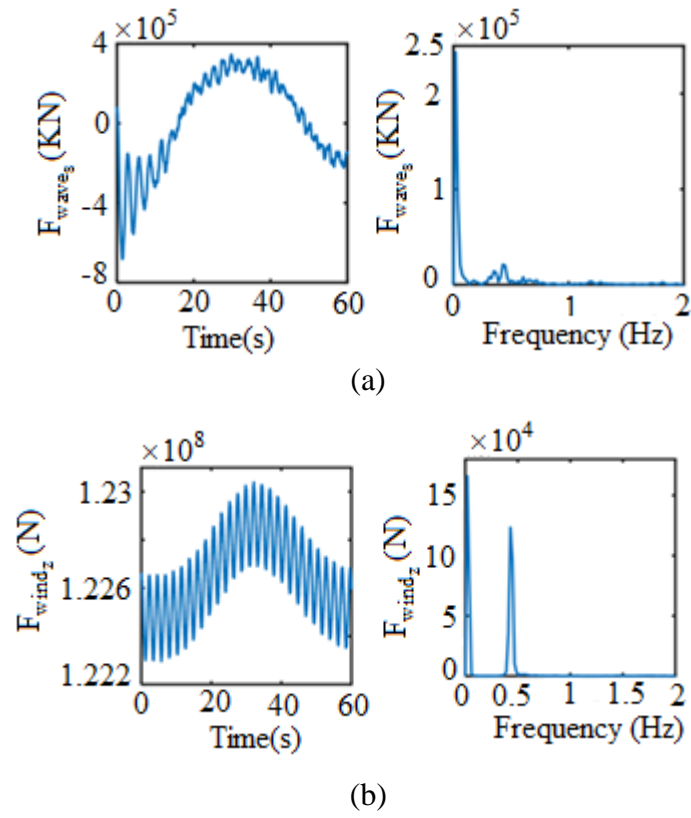
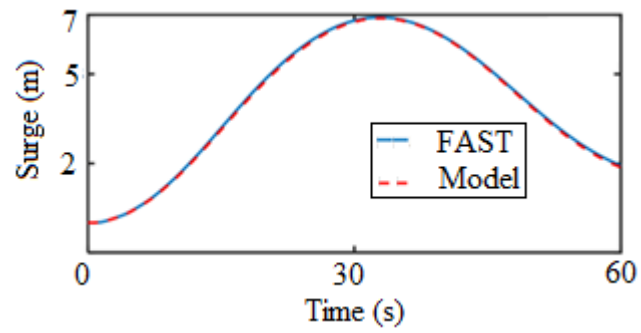
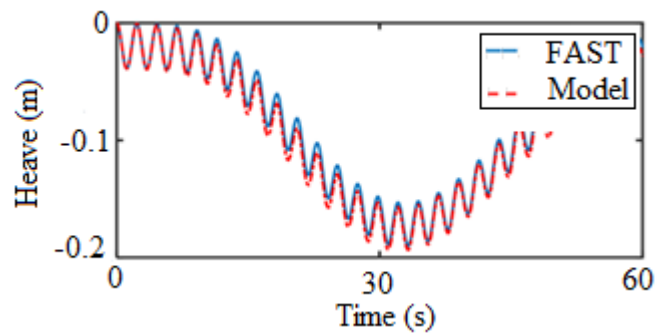


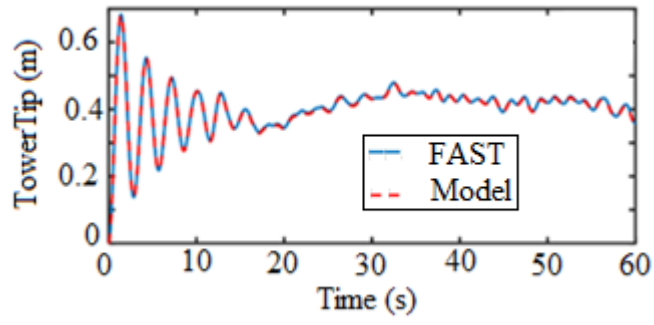
Fig. 3. Time history and FFT of exerted force to the platform (a) in surge direction
(b) in heave direction



(a)



(b)



(c)

Fig. 4. Comparison of the time history of the motions of the FAST (blue solid line) and proposed model (red dashed line).

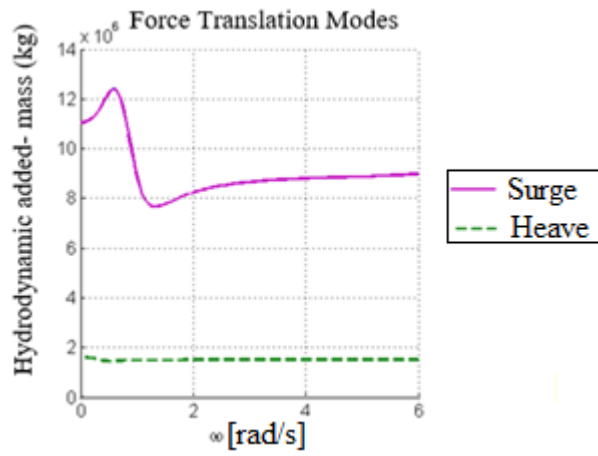
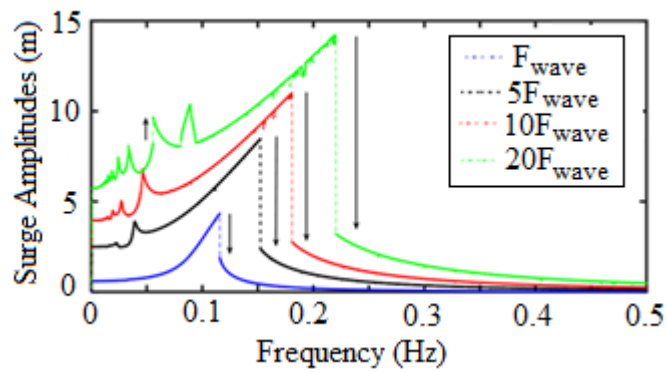
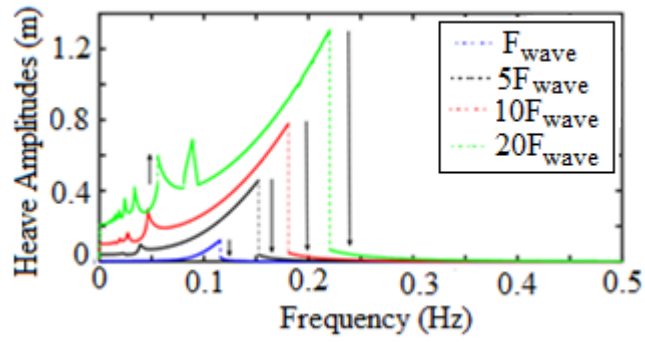


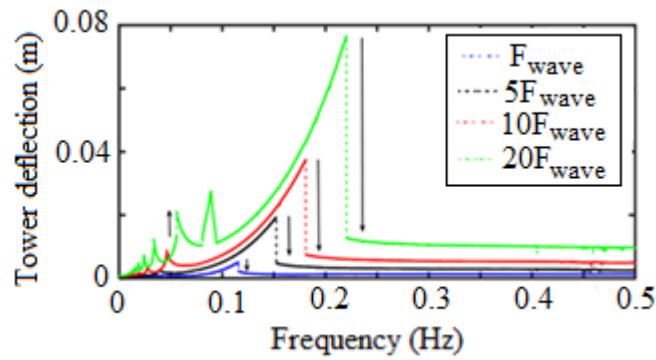
Fig. 5. Hydrodynamic added-mass coefficients of the TLP [50]



(a)

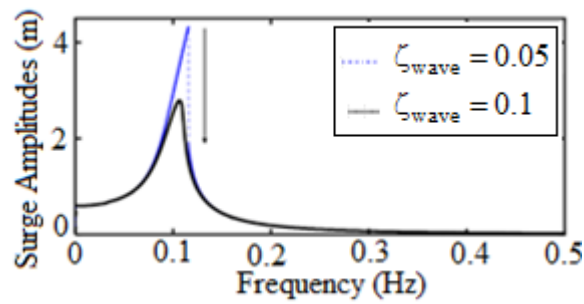


(b)

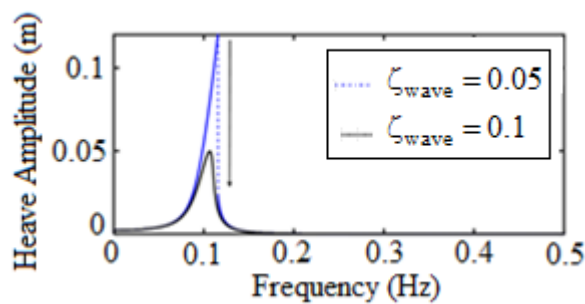


(c)

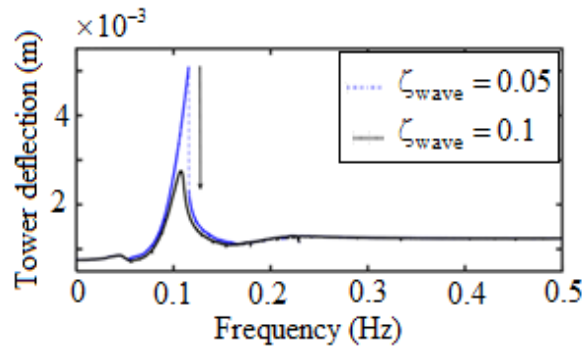
Fig. 6: Frequency response of the (a) surge motions of the offshore wind turbine (b) heave motion (c) deflection of the tower of the offshore wind turbine for increasing the wave forcing F_{wave_s}



(a)

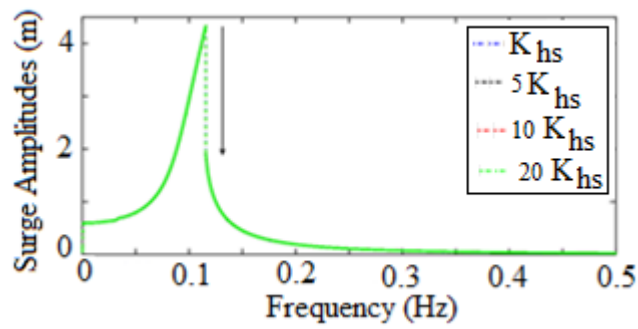


(b)

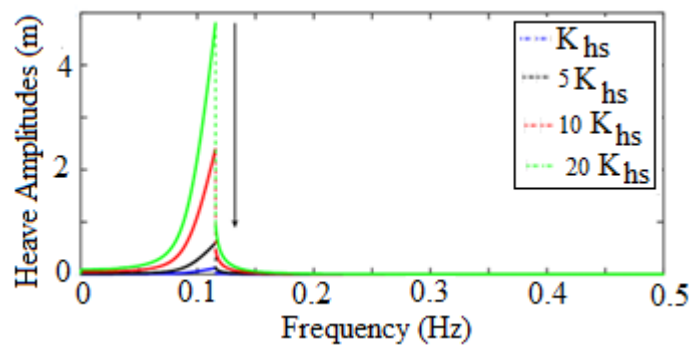


(c)

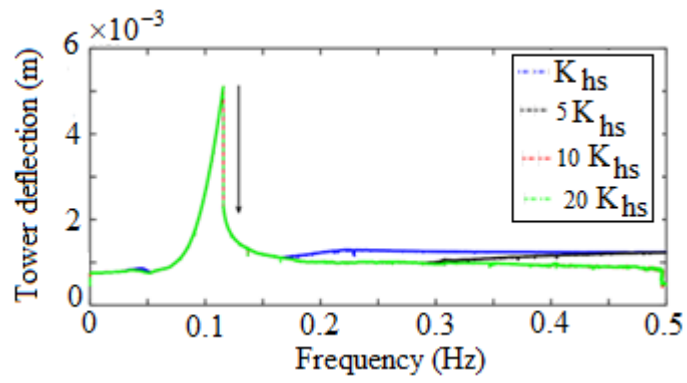
Fig. 7: Frequency response of the (a) surge motions of the offshore wind turbine (b) heave motion (c) deflection of the tower of the offshore wind turbine for various damping in the surge direction.



(a)



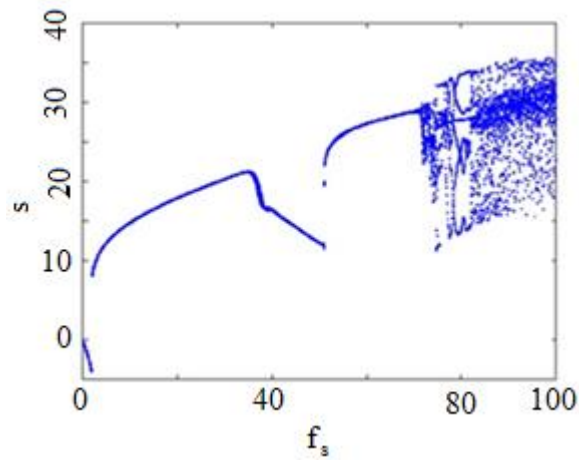
(b)



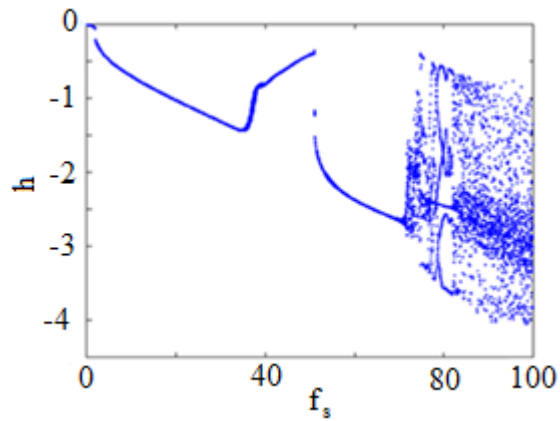
(c)

Fig. 8: Frequency response of the (a) surge motions of the offshore wind turbine (b) heave motion (c) deflection of the tower of the offshore wind turbine for increasing the coupling

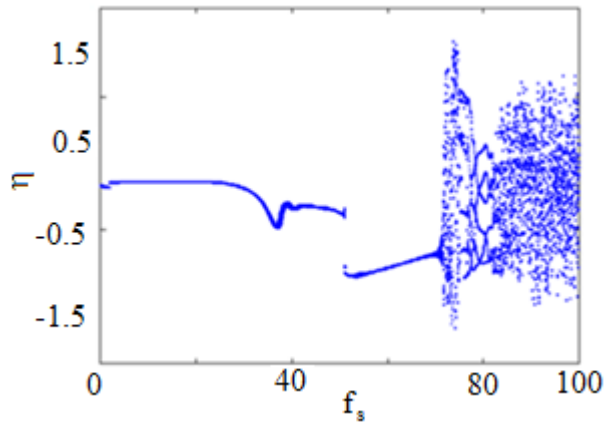
stiffness K_{hs}



(a)



(b)



(c)

Fig. 9: Bifurcation diagrams of Poincaré points for increasing the wave forcing amplitude in the surge direction for (a) surge motions of the offshore wind turbine (b) heave motion (c) deflection of the tower of the offshore wind turbine

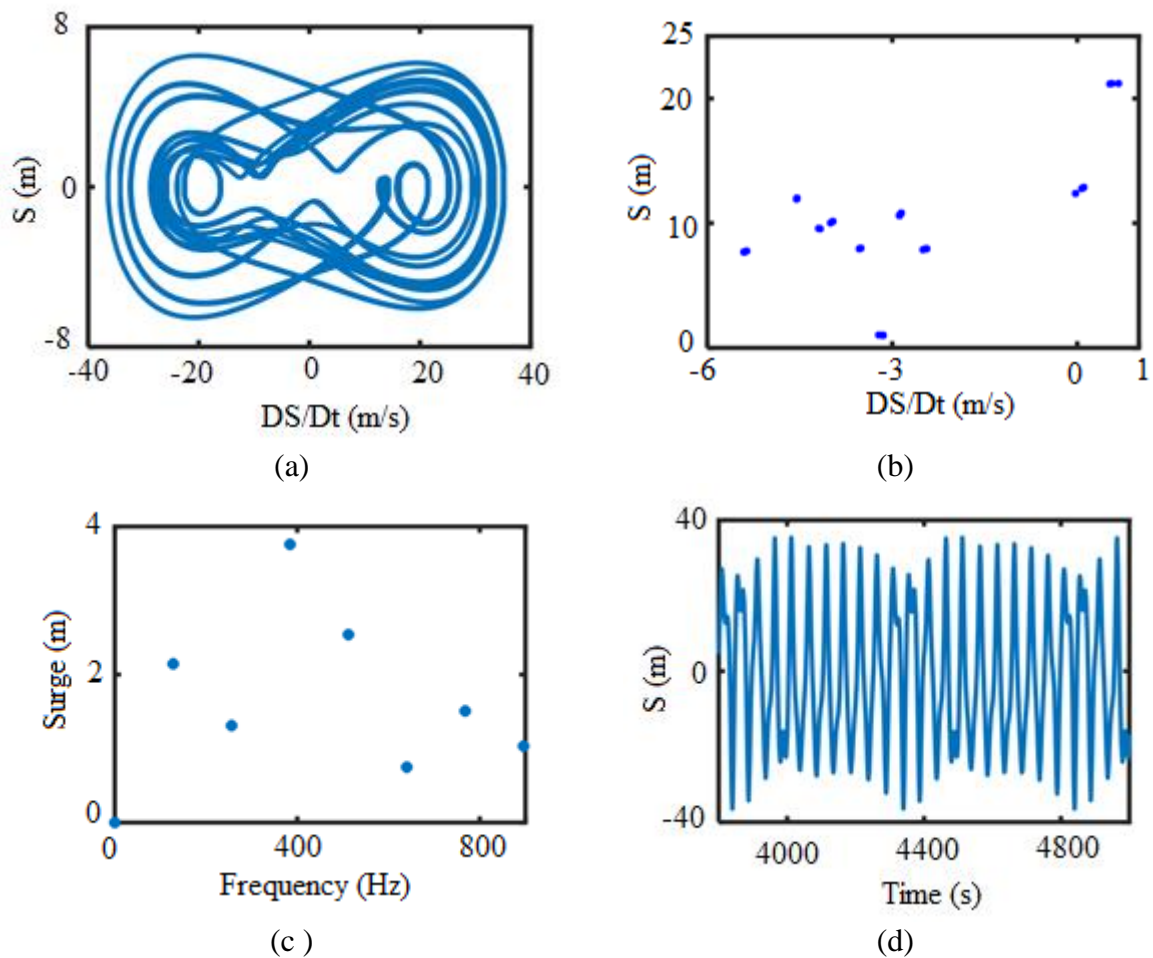
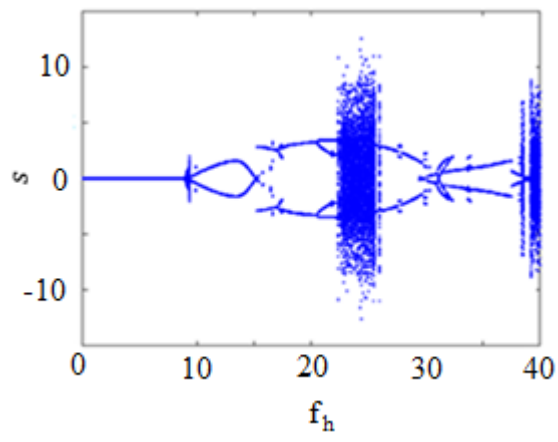
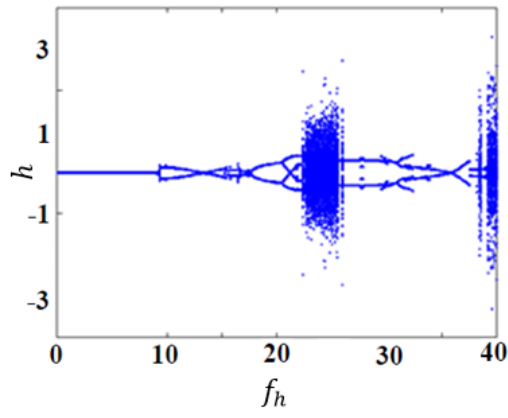


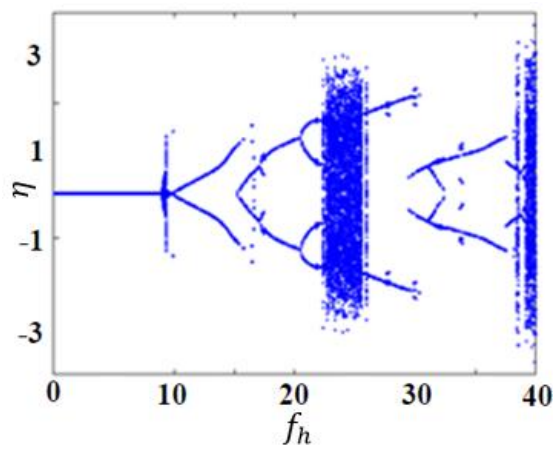
Fig. 10: Chaotic oscillation for the floating offshore wind turbine at $f_s = 83$; (a) phase-plane diagram of the surge motions; (b) Poincaré section of the surge motions, (c) FFT of the surge motions and (d) time history of the surge motions.



(a)



(b)



(c)

Fig. 11: Bifurcation diagrams of Poincaré points for increasing the wave forcing amplitude in the heave direction for (a) surge motions of the offshore wind turbine (b) heave motion (c) deflection of the tower of the offshore wind turbine

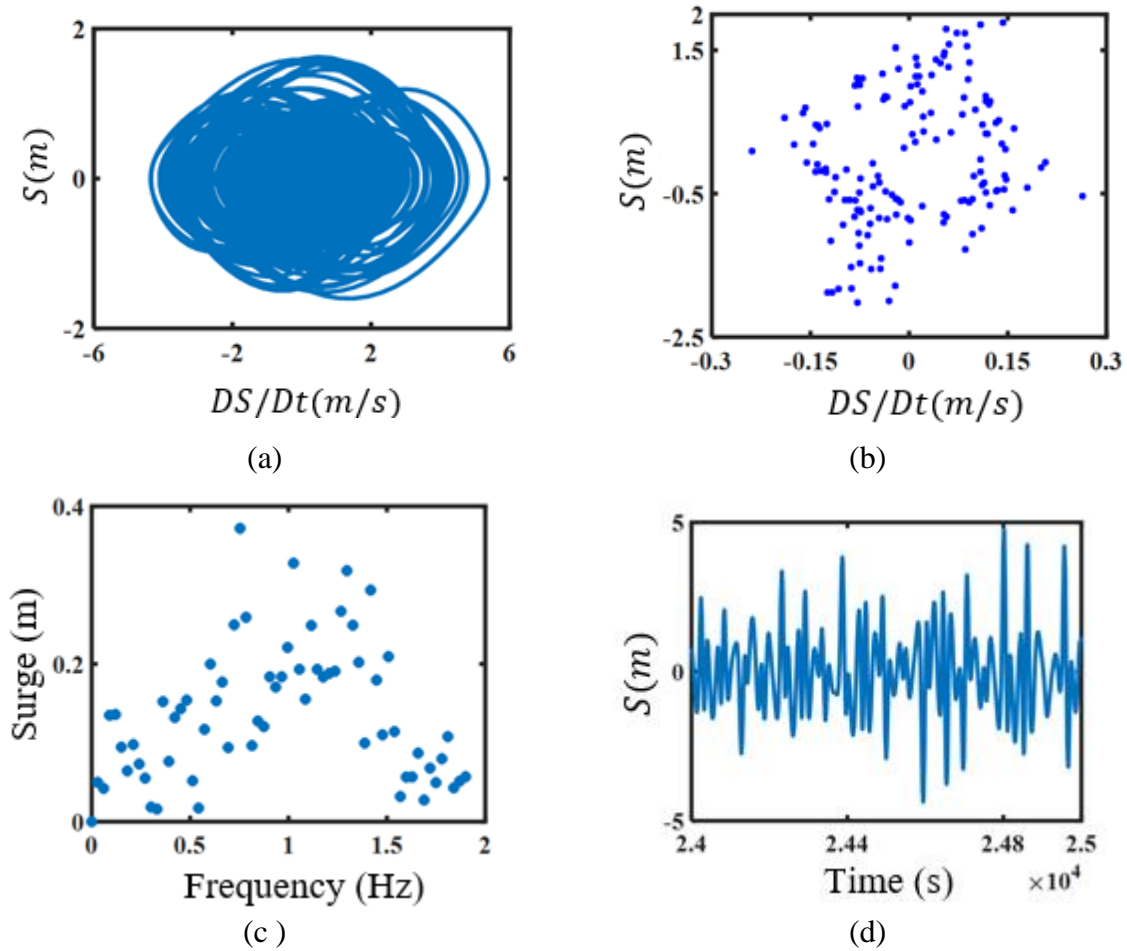
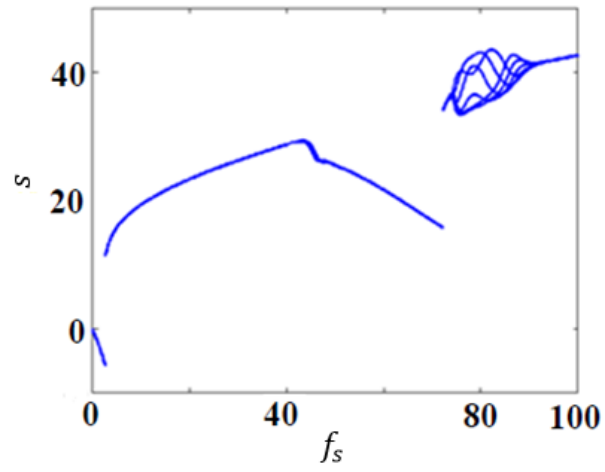
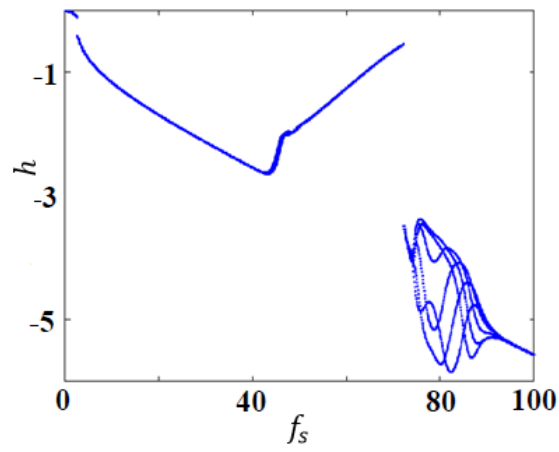


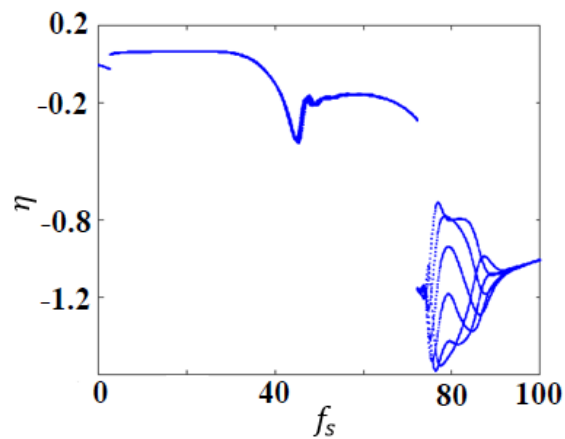
Fig. 12: Chaotic oscillation for the floating offshore wind turbine at $f_h = 9.375$; (a) phase-plane diagram of the surge motion; (b) Poincaré section of the surge motion, (c) FFT of the surge motion and (d) time history of the surge motion.



(a)



(b)



(c)

Fig. 13: Bifurcation diagrams of Poincaré points for increasing the wave forcing amplitude in the surge direction with 30% increase in the length of the mooring lines for (a) surge motions

of the offshore wind turbine (b) heave motion (c) deflection of the tower of the offshore wind turbine

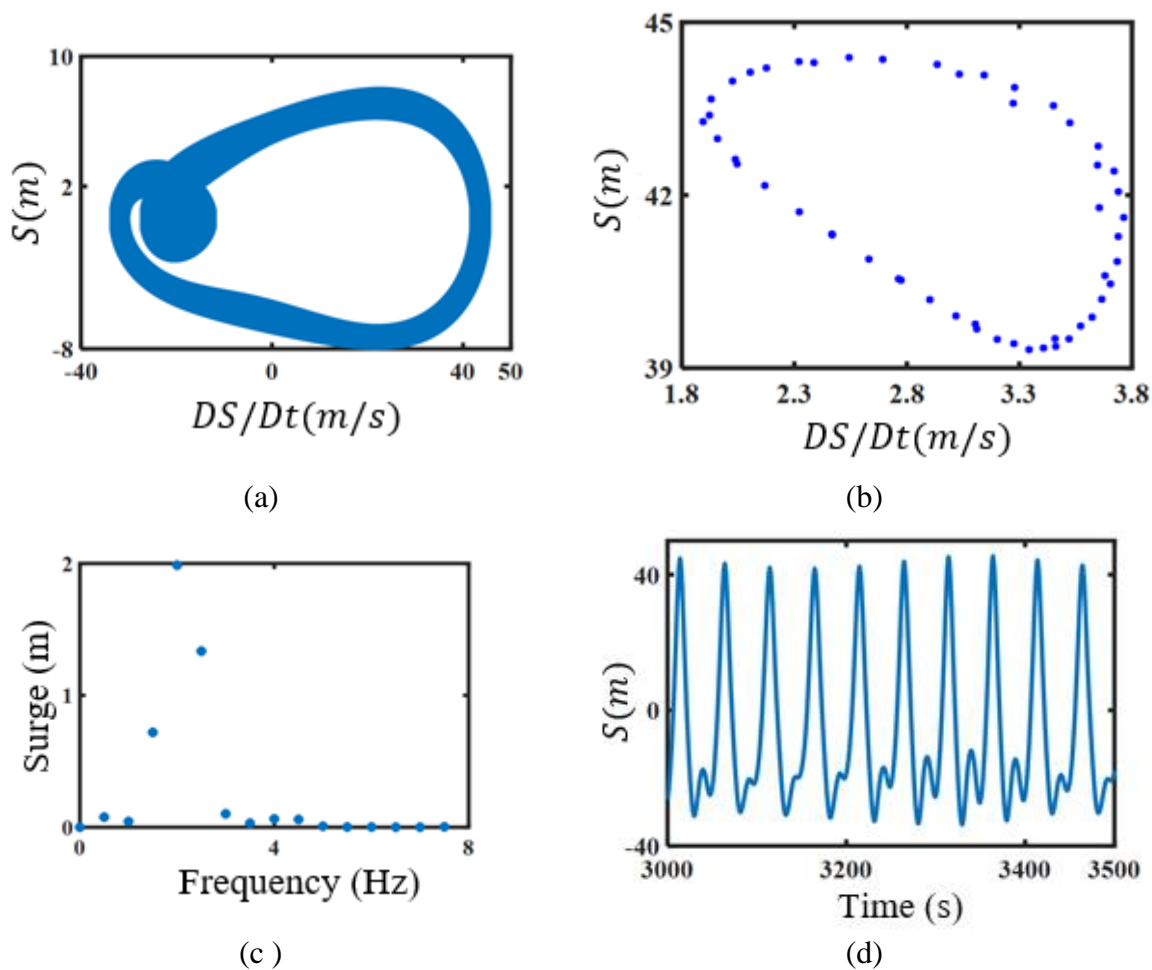
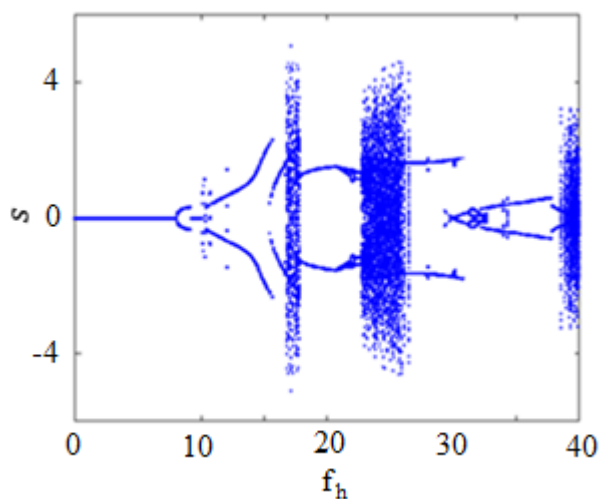
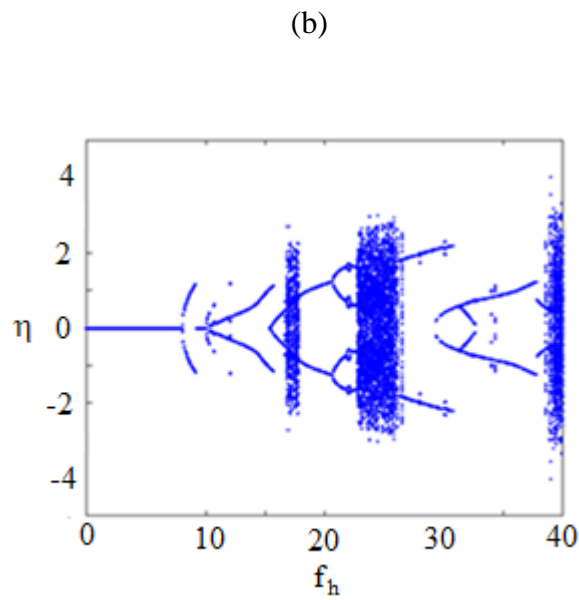
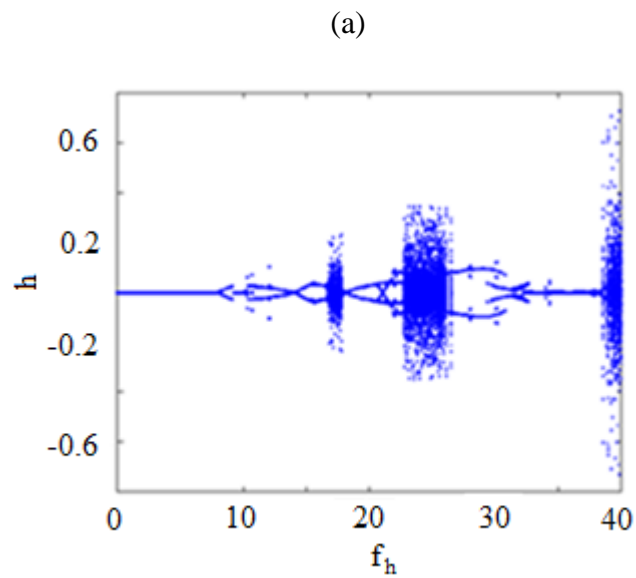


Fig. 14: Quasi-periodic oscillation for the floating offshore wind turbine with 30% increase in the length of the mooring lines at $f_s = 85$; (a) phase-plane diagram of the surge motions; (b) Poincaré section of the surge motions, (c) FFT of the surge motions and (d) time history of the surge motions.





(c)

Fig. 15: Bifurcation diagrams of Poincaré points for increasing the wave forcing amplitude in the heave direction with increase in the length of the mooring lines for (a) surge motions of the offshore wind turbine (b) heave motion (c) deflection of the tower of the offshore wind turbine

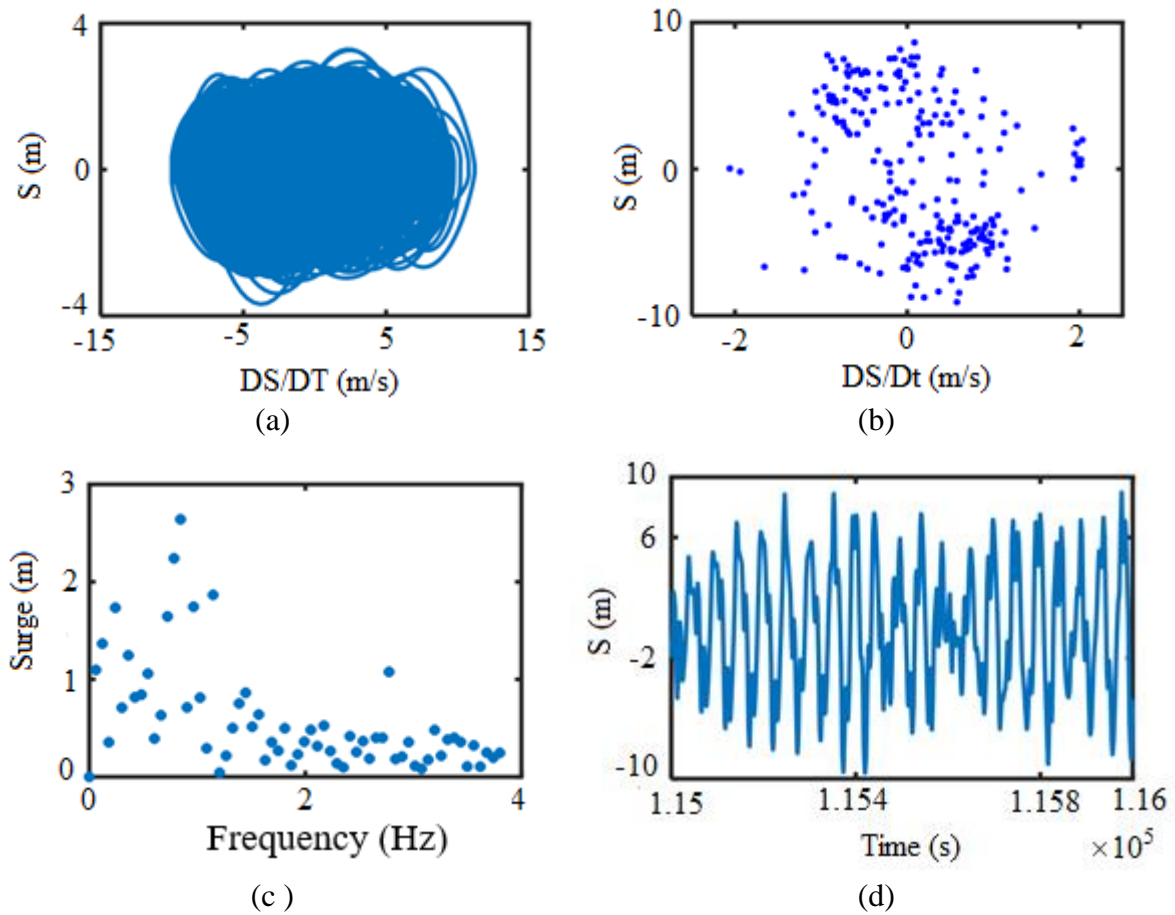
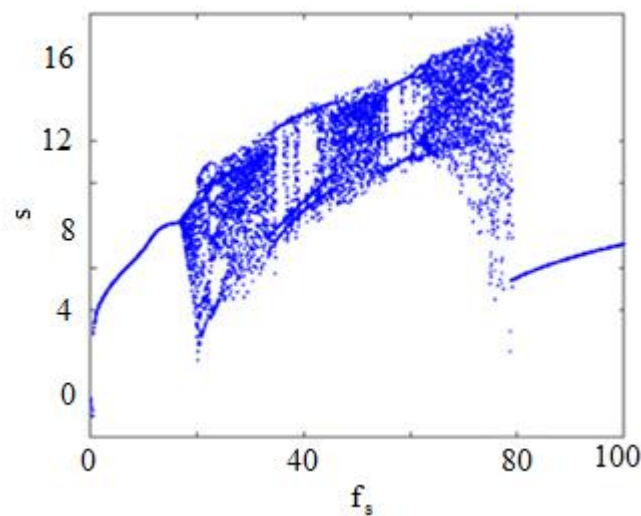
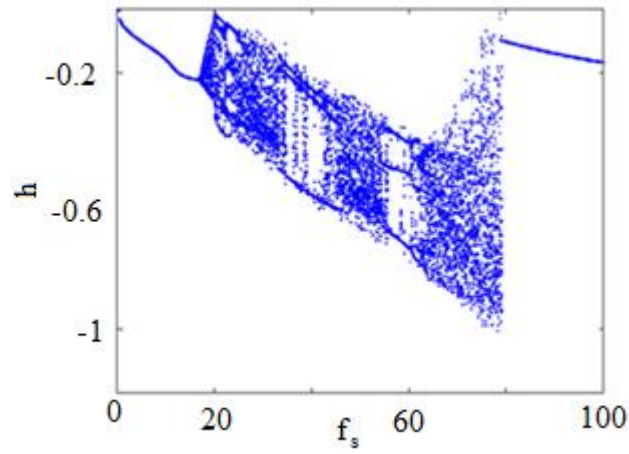


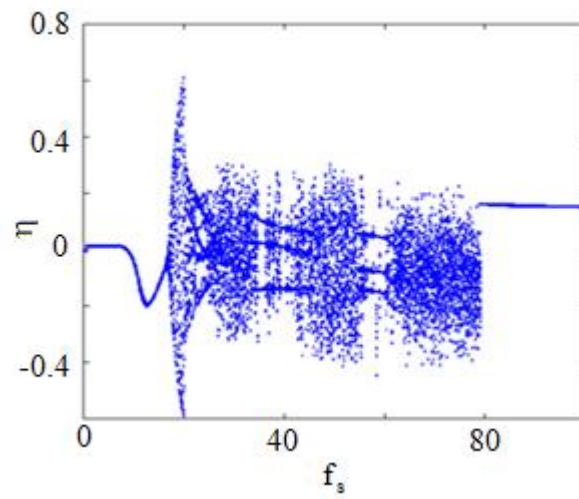
Fig. 16: Chaotic oscillation for the floating offshore wind turbine with 30% increase in the length of the mooring lines at $f_h = 17.3$; (a) phase-plane diagram of the surge motion; (b) Poincaré section of the surge motion, (c) FFT of the surge motion and (d) time history of the surge motion.



(a)

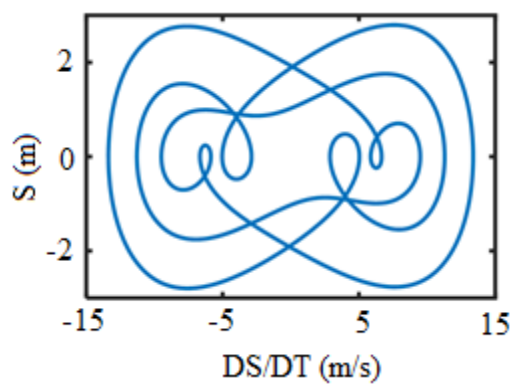


(b)

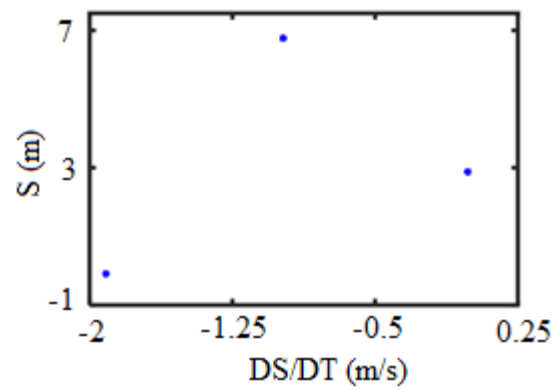


(c)

Fig. 17: Bifurcation diagrams of Poincaré points for increasing the wave forcing amplitude in the surge direction with 50% decrease in the length of the mooring lines for (a) surge motions of the offshore wind turbine (b) heave motion (c) deflection of the tower of the offshore wind turbine



(a)



(b)

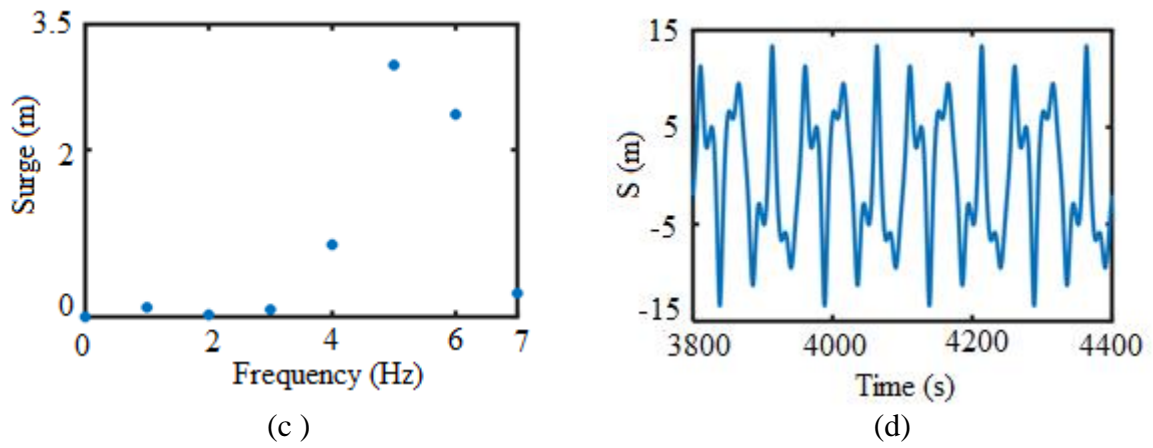
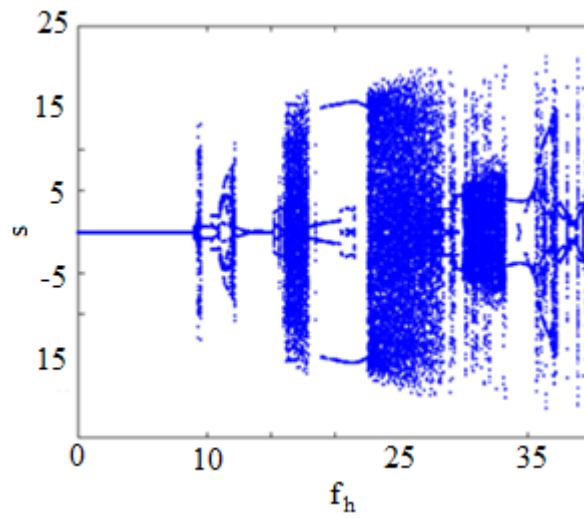
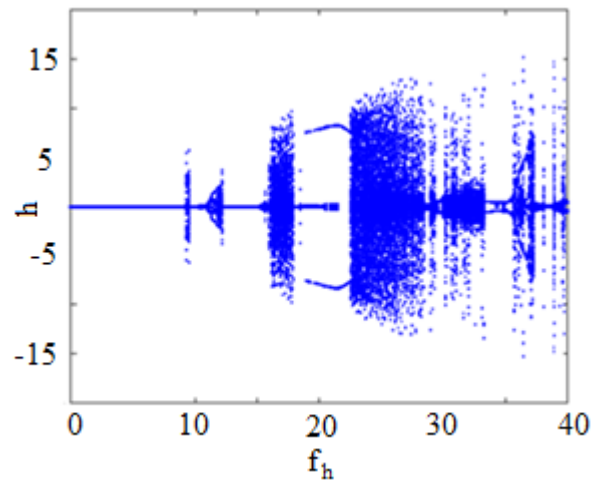


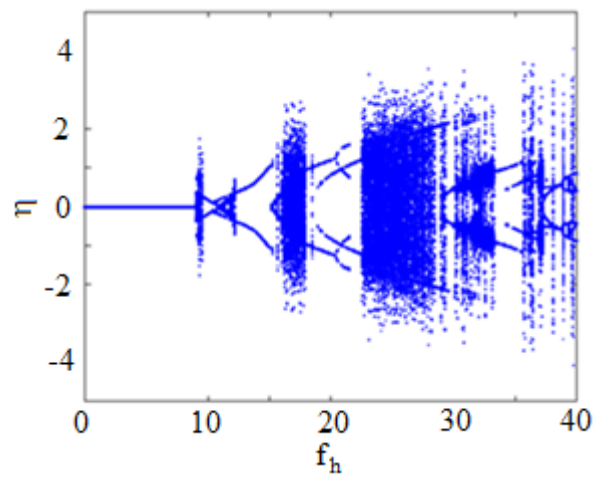
Fig. 18: Periods-3 oscillation for the floating offshore wind turbine with 50% reduction in the length of the mooring lines at $f_s = 39.84$; (a) phase-plane diagram of the surge motions; (b) Poincaré section of the surge motions, (c) FFT of the surge motions and (d) time history of the surge motions.



(a)



(b)



(c)

Fig. 19: Bifurcation diagrams of Poincaré points for increasing the wave forcing amplitude in the heave direction with 50% reduction in the length of the mooring lines for (a) surge motions of the offshore wind turbine (b) heave motion (c) deflection of the tower of the offshore wind turbine

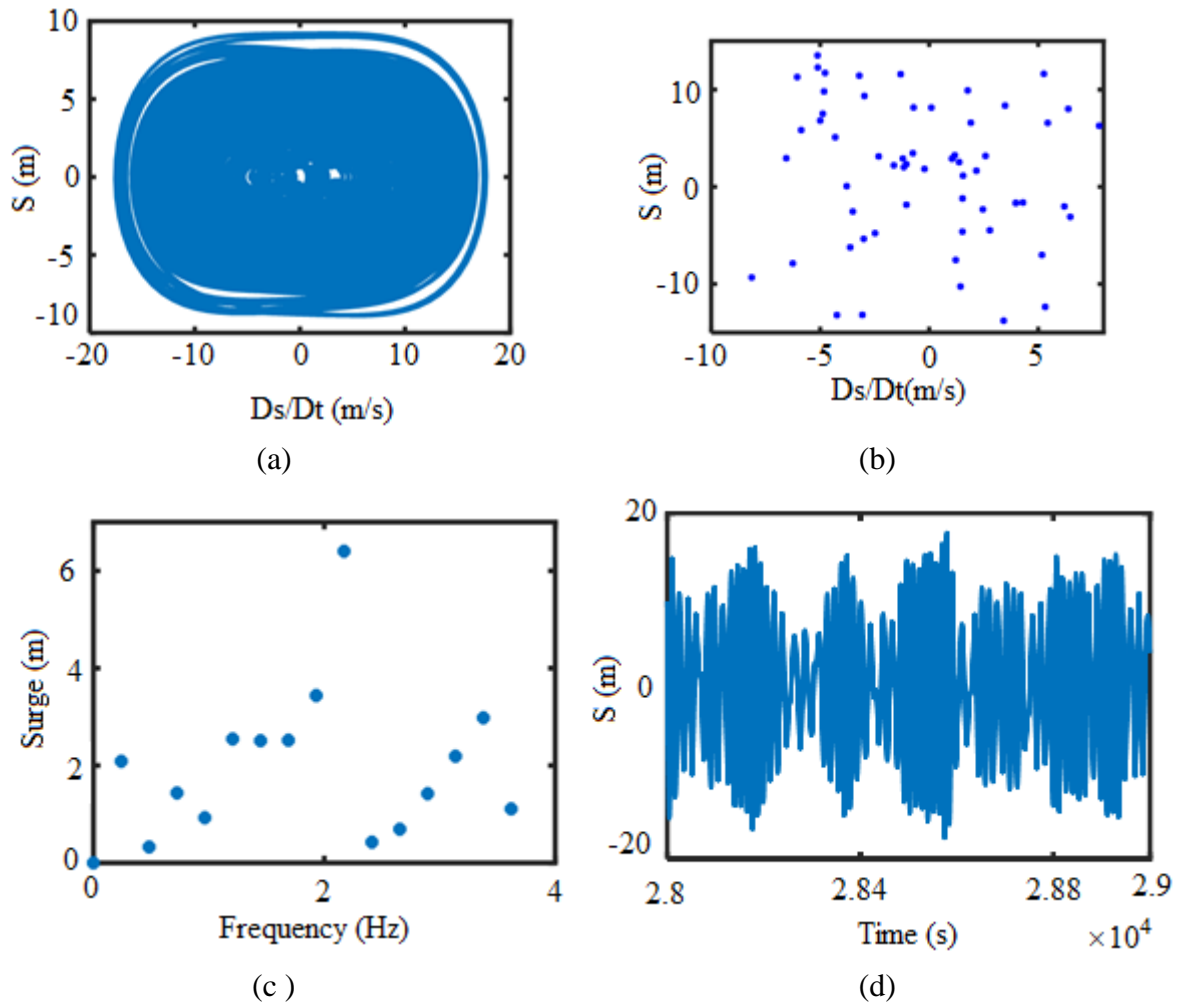


Fig. 20: Chaotic oscillation for the floating offshore wind turbine with 50% reduction in the length of the mooring lines at $f_h = 16.2$; (a) phase-plane diagram of the surge motion; (b) Poincaré section of the surge motion, (c) FFT of the surge motion and (d) time history of the surge motion.

Table 1. Summary of the properties for the NREL 5 MW baseline wind turbine [41].

Rating (MW)	5
Rotor orientation, configuration	Upwind, 3 blades
Control	Variable speed, collective pitch
Drive train	High speed, multiple-stage gearbox
Rotor, hub diameter (m)	126, 3
Hub height (m)	90
Cut-in, rated, cut-out wind.speed (m s ⁻¹)	3, 11.4, 25
Rotor mass (kg)	110,000
Nacelle mass (kg)	240,000

Tower mass (kg)	347.460
Blade second mass of inertia with respect to root (kg.m ²)	11776047
Location of the tower center of mass	38.23
Location of overall center of mass of the WT	0.2 m upwind of tower centerline, 64.0 m above still water level (SWL)

Table 2. Distributed tower properties of the NREL 5 MW baseline wind turbine [41].

Elevation (m)	Mass density (kg / m)	Tower fore-aft stiffness (N)
0.00	5590.87	138.13E+9
8.76	5232.43	129.27E+9
17.52	4885.76	120.71E+9
26.28	4550.87	112.43E+9
35.04	4227.75	104.45E+9
43.80	3916.41	96.7E+9
52.56	3616.83	89.36E+9
61.32	3329.03	82.25E+9
70.08	3053.01	75.43E+9
78.84	2788.75	68.90E+9
87.60	2536.27	62.66E+9

Table 3. Summary of the properties for the MIT/NREL floating platforms [42].

Diameter or width \times length (m)	18
Draft (m)	47.89
Mass (kg)	8600000
CM location of the platform below SWL (m)	40.61
Number of mooring lines	8 (4pairs)
Depth to fairleads, anchors (m)	47.89, 200
Radius to fairleads, anchors (m)	27, 27
Unstretched line length (m)	151.7
Line extensional stiffness (N)	1,500,000,000
Platform added mass in the surge direction(kg)	9E+6 kg

Soheil Ghabraei received the B.Sc., M.Sc. and Ph.D. degrees in mechanical engineering from the Sharif University of Technology in 2013, 2015 and 2023, respectively. His current research interests include system dynamics and nonlinear vibration.

Hamed Moradi received the B.Sc., Mechanical Engineering degree in solid mechanics from Amirkabir University of Technology in 2005; M.Sc. & PhD Mech. Eng. in applied mechanics

from Sharif University of Technology (SUT) in 2008 and 2012. Currently, he is the Associate Professor in the Department of Mechanical Engineering, Sharif University of Technology. His current research interests include the modeling of dynamic systems, application of robust, nonlinear and optimal control methods in various dynamics systems such as manufacturing, bio-engineering, thermo-fluid industrial processes, renewable energy and power plant engineering